

Article

Development and Intercomparison Study of an Atmospheric Motion Vector Retrieval Algorithm for GEO-KOMPSAT-2A

Soo Min Oh ^{1,2} , Régis Borde ³, Manuel Carranza ⁴ and In-Chul Shin ^{2,*}

¹ Department of Physics and Astronomy, Seoul National University, 1, Gwanak-ro, Gwanak-gu, Seoul 08826, Korea

² Satellite Development Division, National Meteorological Satellite Center, Jincheon 27803, Korea

³ EUMETSAT, Eumetsat Allee 1, 64295 Darmstadt, Germany

⁴ GMV INSYEN at EUMETSAT, Eumetsat Allee 1, 64295 Darmstadt, Germany

* Correspondence: icshin@korea.kr

Received: 31 July 2019; Accepted: 29 August 2019; Published: 1 September 2019



Abstract: We derived an atmospheric motion vector (AMV) algorithm for the Geostationary Korea Multipurpose Satellite (GEO-KOMPSAT-2A; GK-2A) launched on 4 December 2018, using the Advanced Himawari Imager (AHI) onboard Himawari-8, which is very similar to the Advanced Meteorological Imager onboard GK-2A. This study clearly describes the main steps in our algorithm and optimizes it for the target box size and height assignment methods by comparing AMVs with numerical weather prediction (NWP) and rawinsonde profiles for July 2016 and January 2017. Target box size sensitivity tests were performed from 8×8 to 48×48 pixels for three infrared channels and from 16×16 to 96×96 pixels for one visible channel. The results show that the smaller box increases the speed, whereas the larger one slows the speed without quality control. The best target box sizes were found to be 16×16 for CH07, 08, and 13, and 48×48 pixels for CH03. Height assignment sensitivity tests were performed for several methods, such as the cross-correlation coefficient (CCC), equivalent blackbody temperature (EBBT), infrared/water vapor (IR/WV) intercept, and CO₂ slicing methods for a cloudy target as well as normalized total contribution (NTC) and normalized total cumulative contribution (NTCC) for a clear-air target. For a cloudy target, the CCC method is influenced by the quality of the cloud's top pressure. Better results were found when using EBBT and IR/WV intercept methods together rather than individually. Furthermore, CO₂ slicing had the best statistics. For a clear-air target, the combined use of NTC and NTCC had the best statistics. Additionally, the mean vector difference, root-mean-square (RMS) vector difference, bias, and RMS error (RMSE) between GK-2A AMVs and NWP or rawinsonde were smaller by approximately 18.2% on average than in the case of the Communication, Ocean and Meteorology Satellite (COMS) AMVs. In addition, we verified the similarity between GK-2A and Meteosat Third Generation (MTG) AMVs using the AHI of Himawari-8 from 21 July 2016. This similarity can provide evidence that the GK-2A algorithm works properly because the GK-2A AMV algorithm borrows many methods of the MTG AMV algorithm for geostationary data and inversion layer corrections. The Pearson correlation coefficients in the speed, direction, and height of the prescribed GK-2A and MTG AMVs were larger than 0.97, and the corresponding bias/RMSE were 0.07/2.19 m/s, 0.21/14.8°, and 2.61/62.9 hPa, respectively, considering common quality indicator with forecast (CQIF) > 80.

Keywords: GK-2A; atmospheric motion vector (AMV); Himawari-8; target box size; height assignment; COMS; MTG; intercomparison

1. Introduction

The first atmospheric motion vector (AMV) algorithm from a polar satellite image of the Television Infrared Observation Satellite (TIROS) was developed by Fujita in the 1960s [1]. These accurate inferences of wind have also been used to study cloud motion with geostationary satellite images. In addition, numerous corresponding investigations of geostationary cloud motion have been conducted since the first geostationary cloud motions from the first Applications Technology Satellite were studied in 1966 [2].

Geostationary AMV algorithms based on target selection, height assignment, tracking, and quality control have been recently developed by many institutions, such as the Japan Meteorological Agency [3–5], European Organization for the Exploitation of Meteorological Satellites (EUMETSAT) [6–8], and the National Oceanic and Atmospheric Administration/National Environmental Satellite Data and Information Service (NOAA/NESDIS) [9–12]. The first Korean geostationary AMV algorithm [13–16], developed by the Korea Meteorological Administration (KMA), was applied to the meteorological imager (MI) of the Communication, Ocean, and Meteorological Satellite (COMS) launched on 26 June 2010, which was the first generation of geostationary satellites of Korea. In this algorithm, AMVs are derived for the visible channel (VIS) at 0.675 μm shortwave infrared channel (SWIR) at 3.75 μm , and infrared channel (IR) at 10.8 μm over the extended Northern Hemisphere (ENH) region. On 4 December 2018, the GEO-KOMPSAT-2A (GK-2A) satellite in Korea was successfully launched. The Advanced Meteorological Imager (AMI) of GK-2A shows better temporal and spatial resolution than the MI of COMS [17]. There is also plenty of room for improvement in the AMV algorithm when AMI is used because it has 16 channels compared to the MI with 5 channels.

Here, we derive and improve the GK-2A AMV retrieval algorithm by comparing it with the Meteosat Third Generation (MTG) [6–8] AMV retrieval algorithm through the international collaboration with experts at EUMETSAT. The new MTG AMV algorithm is based on the Meteosat Second Generation (MSG) AMV retrieval algorithm of EUMETSAT. Moreover, the GK-2A AMV algorithm follows the main steps of the MTG AMV algorithm for geostationary satellite data based on the COMS AMV algorithm. Thus, we confirm the performance of GK-2A AMVs in comparison with that of the MTG AMVs and the similarity between them. In addition, the performance of the GK-2A AMV is compared with that of the COMS AMVs.

In addition, we derive and optimize our AMV algorithm for GK-2A by using the Advanced Himawari Imager (AHI) [18] of the Himawari-8 satellite, which has properties very similar to those of the AMI. Moreover, we verify the similarity between the GK-2A and MTG AMVs to confirm that our algorithm works properly. Section 2 describes our input data used to produce the GK-2A AMVs and validation data used to verify the performance of this algorithm. The data for the intercomparison of GK-2A and MTG AMVs are also described in this section. In Section 3, our GK-2A algorithm is described in detail, as is the validation method used to estimate the performance of this algorithm. The results of the sensitivity tests on the target box size [19–22] and height assignment methods [23–25], the validation performance comparison between GK-2A AMVs and COMS AMVs, and the intercomparison results between GK-2A and MTG AMVs are described in Section 4. In Section 5, the results are discussed, and the novelty and limitations of this study are described. The summary and conclusions of this study are presented in Section 6. Additionally, the differences in the GK-2A and MTG AMV algorithms are outlined in Appendix A. Tables of results for sensitivity tests of the height assignment method of the GK-2A AMV algorithm are presented in Appendix B. The differences of numerical weather prediction (NWP) used in our algorithm are discussed in the Appendix C.

2. Data

2.1. Datasets for Optimization of the GEO-KOMPSAT-2A Atmospheric Motion Vector (GK-2A AMV) Algorithm

The characteristics of the AHI [18] are very similar to those of the AMI, as shown in Table 1. Therefore, we used the AHI of Himawari-8 on behalf of the AMI of GK-2A during the development period. The GK-2A AMV can be derived for CH03 (0.645 μm), 07 (3.85 μm), 08 (6.25 μm), 09 (6.95 μm), 10 (7.35 μm), 13 (10.45 μm), and 14 (11.20 μm) of the AHI, and each algorithm is independent. All of the employed images include global data over a full-disk area of the AHI. The spatial resolution was 500 m for CH03 and 2 km for the others used in this algorithm. To optimize our algorithm, CH03 and CH07 were used as the VIS and SWIR channels, respectively. CH08 was used as the representative among the three WV channels, CH08, 09, and 10. Additionally, CH13 was used to derive wind for the IR channel in this algorithm because the characteristics of the two IR channels, CH13 and 14, are very similar.

Table 1. Comparisons between characteristics of the Advanced Himawari Imager (AHI) and Advanced Meteorological Imager (AMI).

| Channel Number | AHI | | | AMI | | |
|----------------|--------------------------------------|------------------------------|-------------------------|--------------------------------------|------------------------------|-------------------------|
| | Central Wavelength [μm] | Band Width [μm] | Spatial Resolution [km] | Central Wavelength [μm] | Band Width [μm] | Spatial Resolution [km] |
| 1 | 0.455 | 0.05 | 1.0 | 0.470 | 0.041 | 1.0 |
| 2 | 0.510 | 0.02 | 1.0 | 0.509 | 0.029 | 1.0 |
| 3 | 0.645 | 0.03 | 0.5 | 0.639 | 0.081 | 0.5 |
| 4 | 0.860 | 0.02 | 1.0 | 0.863 | 0.034 | 1.0 |
| 5 | 1.61 | 0.02 | 2.0 | 1.37 | 0.015 | 2.0 |
| 6 | 2.26 | 0.02 | 2.0 | 1.61 | 0.041 | 2.0 |
| 7 | 3.85 | 0.22 | 2.0 | 3.83 | 0.19 | 2.0 |
| 8 | 6.25 | 0.37 | 2.0 | 6.21 | 0.84 | 2.0 |
| 9 | 6.95 | 0.12 | 2.0 | 6.94 | 0.40 | 2.0 |
| 10 | 7.35 | 0.17 | 2.0 | 7.33 | 0.18 | 2.0 |
| 11 | 8.60 | 0.32 | 2.0 | 8.59 | 0.35 | 2.0 |
| 12 | 9.63 | 0.18 | 2.0 | 9.62 | 0.38 | 2.0 |
| 13 | 10.45 | 0.30 | 2.0 | 10.35 | 0.47 | 2.0 |
| 14 | 11.20 | 0.20 | 2.0 | 11.23 | 0.66 | 2.0 |
| 15 | 12.35 | 0.30 | 2.0 | 12.36 | 1.11 | 2.0 |
| 16 | 13.30 | 0.20 | 2.0 | 13.29 | 0.57 | 2.0 |

We used analyses of the Global Data Assimilation and Prediction System (GDAPS) data provided by KMA as the numerical weather prediction (NWP) data. The GDAPS T profiles were used to analyze the inversion layer. Furthermore, brightness temperature profiles, transmittance profiles for cloudy AMVs, and clear-air brightness temperature data for clear-air AMVs simulated by the radiative transfer model (RTM) were used to assign the height of each wind. Version 11.2 of the Radiative Transfer for TIROS Operational Vertical Sounder (RTTOV) [26] was used as the RTM to simulate the brightness temperature from the NWP analyses in this algorithm. The spatial resolution of the GDAPS and RTM data was approximately 17 km. As ancillary data, the cloud detection (CLD), cloud top pressure (CTP) from the GK-2A cloud information developer [17] in Korea, and land–sea mask were used to classify the type of target and to assign the height in this algorithm.

Our study area was the full-disk area of the AHI, as shown in Figure 1. We produced AMVs with three consecutive images with time intervals of 10 min for July 2016 and January 2017 every 12 h. These AMVs were compared with the U and V profiles in the GDAPS from the KMA GDAPS and rawinsonde from the Global Telecommunication System (GTS) for the same periods to estimate the performance of the GK-2A AMV algorithm. In addition, the GK-2A AMVs were compared with the COMS AMVs over the ENH region for the same periods when the target box size was 16×16 .

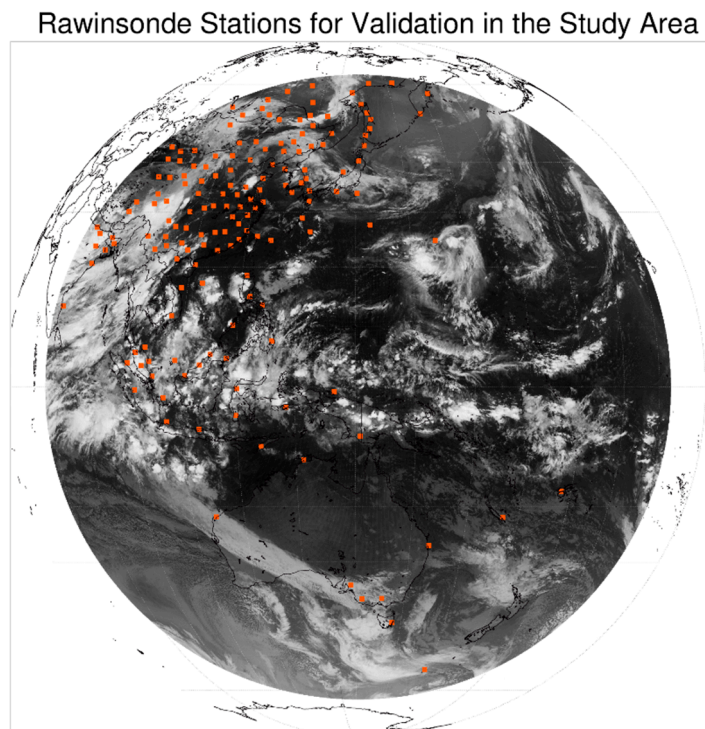


Figure 1. Station information of rawinsonde captured at 12:00 UTC on 21 July 2016. The background plot is the CH13 (10.2 μm) brightness temperature of AHI over our study area. In this full disk area of AHI, the total number of stations is about 160. The nominal time of the rawinsonde launch was 0000 or 1200 UTC, with occasional launches occurring at 06:00 and 18:00 UTC.

2.2. Datasets Used for Intercomparisons of GK-2A and Meteostat Third Generation (MTG) AMV Algorithms

The GK-2A and MTG AMVs were calculated for the prescribed and specific configurations using two triplets of Himawari-8 AHI images captured on 21 July 2016 at the following times to derive the AMVs: 05:30, 05:40, and 05:50 UTC and 12:00, 12:10, and 12:20 UTC. In the prescribed configuration, the GK-2A and MTG AMVs were calculated for the exact same setup configuration. Only the cloudy AMVs with CH13 of the AHI were considered in this case. The target box size and search box size were fixed to 16×16 and 54×54 , respectively. The CTP for the height assignment and CLD data from NOAA/NESDIS were used, as were analyses of the ERA-Interim U , V , and T profiles of the European Centre for Medium-Range Weather Forecasts (ECMWF). The final AMVs were produced with a common quality indicator (QI). In the specific configuration, the GK-2A and MTG AMVs were calculated for their own configurations. The cloudy AMVs with CH03, 07, 08, 10, and 13 of the AHI were considered in this case. For the GK-2A AMVs, the target size and search box size were fixed to 48×48 and 201×201 , respectively, for CH03 with a spatial resolution of 0.5 km. For the other channels, with a spatial resolution of 2 km, the parameters were the same as those in the prescribed configuration. Furthermore, the CTP for height assignment, CLD data from each GK-2A retrieval algorithm, and the analyses of the GDAPS U , V , and T profiles from the KMA were used. The differences of GDAPS and ECMWF are described in Appendix C. Additional heights were calculated by using our own equivalent blackbody temperature (EBBT) [27], IR/water vapor (IR/WV) intercept [7,24], and CO_2 slicing [28,29] methods. In the case of MTG AMVs, the target and search box sizes were 24×24 and 80×80 , respectively, for all channels with a spatial resolution of 2 km. The other input data were the same as those used in the prescribed configuration. The final AMVs were produced with their own QI values each for GK-2A and MTG.

These AMVs were compared with rawinsonde data from GTS and the analyses of GDAPS from the KMA in specific configurations and ERA-Interim ECMWF in prescribed configurations to quantitatively estimate their performance. They were additionally compared with the level 1 profiles of the 532 nm

backscatter return signal and the level 2 profiles of the cloud profile data from the Cloud-Aerosol Lidar with Orthogonal Polarization (CALIOP) product of The Cloud-Aerosol Lidar and Infrared Pathfinder Satellite Observation (CLAIPSO).

3. Methods

3.1. GK-2A AMV Retrieval Algorithm Descriptions

The GK-2A AMV retrieval algorithm was developed individually for the VIS channel (CH03) at 0.645 μm ; SWIR (CH07) at 3.85 μm ; three WV channels (CH08, 09, and 10) at 6.25, 6.95, and 7.35 μm , respectively; and two IR channels (CH13 and 14) at 10.45 and 11.20 μm , respectively, of the AHI over the corresponding full-disk region. Each algorithm comprised four main steps including target selection, height assignment, tracking, and quality control, as shown in Figure 2. After the size of the target was decided, the targets were selected and classified into cloudy and clear-air targets in the target selection step. In the height assignment step, different methods were adopted for the cloudy and clear-air targets including the cross-correlation coefficient (CCC) [30], EBBT, IR/WV intercept, and CO₂ slicing methods for the cloudy target and normalized total contribution (NTC) and normalized total cumulative contribution (NTCC) for the clear-air target. If an inversion layer was present, the final height could be modified by using the inversion layer-correction method. In the tracking step, the speed and direction of each target were calculated by using the CCCs between three consecutive satellite images with an interval of 10 min; this method is defined in [7] as the cross-correlation (CC) method. Finally, two quality flags of the vectors were estimated in the quality control step: the first is the QI developed by EUMETSAT [31] and the second is the expected error (EE) developed by the Bureau of Meteorology Australia. In this section, we describe the input data of our algorithm and provide a detailed description of the four main steps.

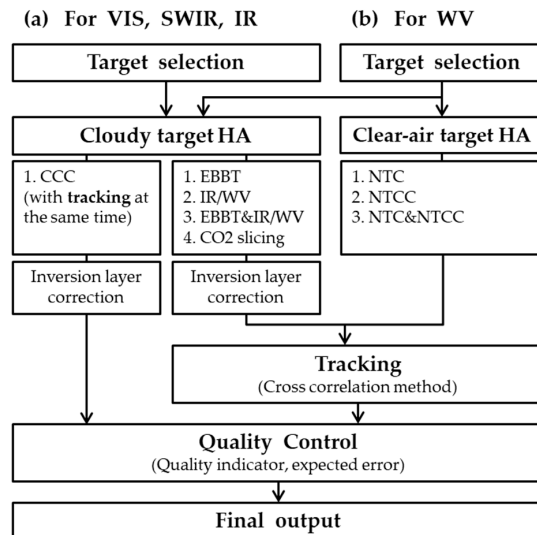


Figure 2. Flowchart of the GEO-KOMPSAT-2A atmospheric motion vector (GK-2A AMV) retrieval scheme. The GK-2A AMV algorithm consists of four main steps such as target selection, height assignment, tracking, and quality control. (a) For visible (VIS) (CH03), shortwave infrared (SWIR) (CH07), and two infrared (IR) channels (CH13 and 14), there are only cloudy AMVs. But (b) for three water vapor (WV) channels (CH08, 09, and 10), there are both cloudy and clear-air AMVs. If the type of target is decided after target selection, different height assignment methods are adopted whether it is cloudy or clear. For a cloudy target, inversion layer correction is carried out additionally. After that, speed and direction are calculated in the tracking process using the cross-correlation (CC) method. Just for the cross-correlation coefficient (CCC) case, height assignment and tracking processes are conducted at the same time. Finally, quality indicator (QI) and expected error (EE) values of each vector are calculated to estimate the quality.

3.1.1. Target Selection

Target selection is the first step of the AMV retrieval scheme. We used the middle of the three consecutive satellite images in this process. After the size of each target was decided, the targets were divided into 3×3 boxes. Then, the mean and standard deviation of the nine pixels within these boxes regarding the brightness temperature for SWIR, IR, and WV or the albedo for VIS were computed. Following this, we moved the center of the target to the center of the box with the largest standard deviation among the candidates for all boxes, as shown in Figure 3. If the largest standard deviation of targets was below a given threshold, they failed to be final targets because they were too coherent to track. As a result of this process, the final targets to be analyzed were decided. Moreover, the distance between each target was the same as the width of the target box area. In addition, the targets for the VIS (SWIR) channel were valid only for solar zenith angles $<85^\circ$ ($>90^\circ$).

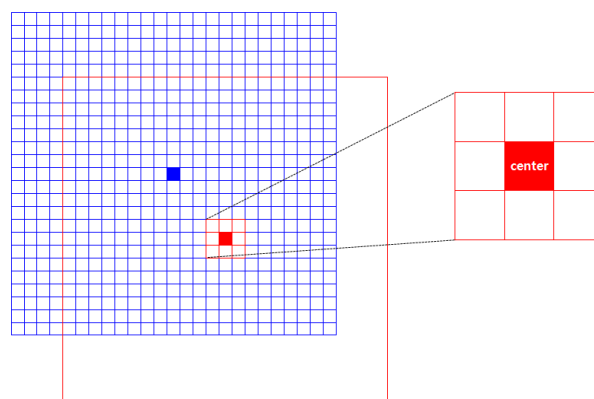


Figure 3. Example of a change in target center in the target selection process for a given target box size. The original center of 25×25 pixels of the blue target box moves to the new center of 3×3 pixels of the red nested box with the largest standard deviation of nine pixels in brightness temperature for SWIR, IR, and WV or albedo for VIS.

These targets were divided into cloudy and clear-air types. If more than 80% of the total number of pixels in the target were cloudy, the cloudy type was assigned. However, for the WV channels, the cloudy type was assigned only if the height of the target was higher than the threshold height, which was a transmittance of 0.4. If fewer than 20% of the total number of pixels in the target were cloudy, the clear-air type was assigned. However, for the WV channels, clear-air type also applied if more than 20% of the total number of pixels in the target were cloudy but the height of the target was lower than the threshold height, which was a transmittance of 0.0001 [32].

3.1.2. Height Assignment

Height assignment methods were applied according to the target type. Accordingly, CCC, EBBT, IR/WV intercept, the combined EBBT and IR/WV intercept, and CO_2 slicing methods can be applied for the cloudy target, and NTC, NTCC, and the combined NTC and NTCC methods can be used for the clear-air target. Moreover, inversion layer correction was used only for cloudy AMVs. The details are described as follows.

(1) For cloudy AMVs

(a) CCC

First, we must identify the target in the second image that best matches that in the first or third image. CCC is used as the degree of matching between two images, A and B. These CCC values are calculated for the corresponding search area in the first or third image as follows:

$$CC_{m,n} = \frac{1}{MN} \sum_{j=1}^N \sum_{i=1}^M CC_{i,j} = \frac{1}{MN} \sum_{j=1}^N \sum_{i=1}^M \left(\frac{a_{i,j} - \bar{a}}{\sigma_a} \frac{b_{m+i,n+j} - \bar{b}_{m,n}}{(\sigma_b)_{m,n}} \right) \quad (1)$$

where $CC_{m,n}$ is the CCC at the m -th row and n -th column of the search area at time $t \pm \Delta t$; $CC_{i,j}$ is the individual contribution component; M and N are the length and width size of the target box, respectively; $a_{i,j}$ is the brightness temperature at the i -th row and j -th column of the target box at time t ; \bar{a} and σ_a are the average and standard deviation of all brightness temperatures of the target area at t , respectively; $b_{m+i,n+j}$ is the brightness temperature at the i -th row and j -th column around the m -th row and n -th column of the search area at time $t \pm \Delta t$; and $\bar{b}_{m,n}$ and $(\sigma_b)_{m,n}$ are the average and standard deviation of all brightness temperatures of an M by N target box at the m -th row and n -th column of the search area at t , respectively. The albedo is used for VIS in place of the brightness temperature.

For the largest CCC among these, the height is the weighted average of the CTPs by their individual contribution to $CC_{i,j}$ in the target box in the second image at time t . Only cloudy pixels with $CC_{i,j}$ larger than their average are valid for calculating the final height. In addition, pixels with brightness temperatures lower than their average are valid for all IR channels and pixels, whereas albedo values larger than average are valid for the VIS channel.

(b) EBBT

EBBT is the oldest method used for assigning heights to cloudy targets of the opaque clouds [27]. Assuming that the mean of the coldest 20% cloudy pixels of the IR channel's brightness temperature for the target box represents the top temperature of the opaque cloud, the height is determined to be the best-fit level among the IR channel vertical temperature profiles simulated from the numerical forecast data. The 10.2 μm brightness temperature simulated by RTM was obtained with analyses of GDAPS. In particular, a final height lower than 800 hPa was corrected by the cloud base correction [33,34]. This correction assumes that low-level clouds are usually moved by wind at the bottom level of the clouds. After the standard deviation is multiplied by $\sqrt{2}$ of 10.2 μm brightness temperature in a target and is added to the cloud top temperature, the final height is determined again from the EBBT method using this new temperature. This method is not valid for determining the heights of semitransparent cirrus clouds [28].

(c) IR/WV intercept

The IR/WV intercept method is suitable for semitransparent cloudy targets at upper levels. Therefore, it is adopted only if the final height is higher than the threshold height of 500 hPa. The equation is

$$\frac{R(WV) - R_{cl}(WV)}{R(IR) - R_{cl}(IR)} = \frac{N_\varepsilon(WV)[R(WV, P_c) - R_{cl}(WV)]}{N_\varepsilon(IR)[R(IR, P_c) - R_{cl}(IR)]} \quad (2)$$

The left-hand side of the equation is the ratio between the difference of the cloudy brightness temperature $R(WV)$ and clear-sky brightness temperature $R_{cl}(WV)$ for the WV channel and the difference of the cloudy brightness temperature $R(IR)$ and clear-sky brightness temperature $R_{cl}(IR)$ for the IR channel in a target. The right hand-side is the ratio between the difference of the cloudy brightness temperature $R(WV, P_c)$ simulated by RTM at the corresponding height P_c and clear-sky brightness temperature $R_{cl}(WV)$ for the WV channel and the difference of the cloudy brightness temperature $R(IR, P_c)$ simulated by RTM at the corresponding height P_c and clear-sky brightness temperature $R_{cl}(IR)$ for the IR channel in a target. This method assumes that these two ratios are linearly related. Furthermore, $N_\varepsilon(WV)$ and $N_\varepsilon(IR)$ are the emissivity of the WV and IR channels, respectively. Assuming that the emissivity of the WV and IR channels is almost the same, Equation (2) becomes

$$\frac{R(WV) - R_{cl}(WV)}{R(IR) - R_{cl}(IR)} = \frac{R(WV, P_c) - R_{cl}(WV)}{R(IR, P_c) - R_{cl}(IR)} \quad (3)$$

This means that the slope between the warm and cold points from observation is equal to that from the RTM simulated data. To solve this equation, we used the intersection of the fitting line of the WV and IR channels' brightness temperatures from the AHI and the curve of the WV and IR channels' brightness temperatures simulated by using RTM according to each height. If two intersection points were present, the final height for the cold point was adopted. CH13 and CH09 of the AHI were used as the WV and IR channels, respectively.

(d) EBBT and IR/WV intercept

The method combining the EBBT and IR/WV intercept is used for a cloudy target. If the Pearson correlation coefficient of all pixels in the cloudy target is larger than 0.80, it is considered to be a semitransparent type of cloudy target, and the IR/WV intercept height is adopted. Otherwise, it is considered to be an opaque type of cloudy target, and the EBBT height is adopted.

(e) CO₂ slicing

The CO₂ slicing method is suitable for both opaque and semitransparent clouds. The general equation for this method is very similar to that of the IR/WV intercept method:

$$\frac{R(\text{CO}_2) - R_{cl}(\text{CO}_2)}{R(\text{IR}) - R_{cl}(\text{IR})} = \frac{N_\varepsilon(\text{CO}_2)[R(\text{CO}_2, P_c) - R_{cl}(\text{CO}_2)]}{N_\varepsilon(\text{IR})[R(\text{IR}, P_c) - R_{cl}(\text{IR})]} \quad (4)$$

This method is based on the brightness temperature ratio between the CO₂ and IR channels. The left-hand side is from the AHI, whereas the right-hand side is from the RTM simulated data. If we use two channels with central wavelengths very close in value, we can assume that the emissivity for these two channels is considered to be identical. Then, Equation (4) becomes

$$\frac{R(\text{CO}_2) - R_{cl}(\text{CO}_2)}{R(\text{IR}) - R_{cl}(\text{IR})} = \frac{R(\text{CO}_2, P_c) - R_{cl}(\text{CO}_2)}{R(\text{IR}, P_c) - R_{cl}(\text{IR})} \quad (5)$$

The final height is adopted when these two ratios are identical. CH16 and CH15 of the AHI were used as the CO₂ and IR channels, respectively.

(f) Inversion layer correction

For all methods applied for cloudy AMVs, the final pressure height is lower than 600 hPa; hence, we modified the height by using the inversion layer correction method. If an inversion layer was present, its bottom pressure P_b and top pressure P_t were determined, and the modified height P_{Inv} was calculated between P_b and P_t as follows:

$$P_{Inv} = \frac{C_b P_b + C_t P_t}{C_b + C_t} + C, \quad (6)$$

where nominally $C_b = 2$, $C_t = 1$, and $C = 0$ [35]. If no inversion layer was present, or the modified height was higher than the original height, the final height was not changed.

(2) For clear-air AMVs

(a) NTC

Unlike that from most IR channels, the radiance observed from the WV channel is determined from the radiance emitted in the atmospheric water vapor layers. Therefore, the transmittance profile simulated using the RTM was used to assign the height of water vapor. The height at which this transmittance value is the largest among the levels was adopted as the final height in the NTC method.

(b) NTCC

Similar to the NTC method, the height at which the cumulative transmittance value is equal to 0.5 among the levels was adopted as the final height.

(c) NTC and NTCC

The method combining NTC and NTCC was used for a clear-air target. First, we calculated the heights from both the NTC and NTCC. Then, the higher value was adopted based on the fact that observation from a geostationary satellite tends to represent the top of the cloud or water vapor.

3.1.3. Tracking

In this process, three consecutive images were used. The backward vector between the first and second images and the forward vector between the second and third images were identified. We determined where each target in the second image had been in the first image and where it moved in the third image, respectively. For image processing, we used the CC method. First, the displacement between the pixel with the largest standard deviation in the second image and that with the largest CC value in the corresponding search area in the first or third image was calculated. Each vector was equal to this displacement divided by the time interval between the two consecutive images. The final vector was the average of these backward and forward vectors. The size of the search area in the first and third images was determined from the possible maximum speed chosen.

3.1.4. Quality Control

In this algorithm, the QI and EE values are used as a quality flag of each vector. To obtain the final QI, we calculated the weighted average of five components including speed consistency QI_{SPD} , direction consistency QI_{DIR} , and vector consistency QI_{VEC} between the backward and forward vectors, first-guess consistency QI_{FC} between the final AMV and the first-guess vector, and the spatial consistency QI_{LC} between the final AMV and the surrounding vectors, as given by

$$QI_{SPD} = 1 - \left(\tanh \left(\frac{|Diff_{SPD}|}{\text{MAX}(S_1 * Vel_{SPD}, S_1') + S_2} \right) \right)^{S_3}, \quad (7)$$

where $Diff_{SPD} = SPD_{Backward} - SPD_{Forward}$; $Vel_{SPD} = (SPD_{Backward} + SPD_{Forward})/2.0$; coefficients S_1 , S_1' , S_2 , and S_3 are 0.2, 0.01, 1.0, and 2.5, respectively; SPD represents the speed of the vector; and the subscripts Backward and Forward denote the backward vector and forward vector between the three consecutive satellite images;

$$QI_{DIR} = 1 - \left(\tanh \left(\frac{|Diff_{DIR}|}{D_1 * \exp\left(-\frac{Vel_{DIR}}{D_2}\right) + D_2'} \right) \right)^{D_3}, \quad (8)$$

where $Diff_{DIR} = DIR_{Backward} - DIR_{Forward}$; $Vel_{DIR} = (SPD_{Backward} + SPD_{Forward})/2.0$; coefficients D_1 , D_2 , D_2' , and D_3 are 20.0, 10.0, 10.0, and 4.0, respectively; and DIR represents the direction of the vector;

$$QI_{VEC} = 1 - \left(\tanh \left(\frac{Diff_{VEC}}{\text{MAX}(V_1 * Ave_{VEC}, V_1') + V_2} \right) \right)^{V_3}, \quad (9)$$

where $Diff_{VEC} = \sqrt{(U_{Backward} - U_{Forward})^2 + (V_{Backward} - V_{Forward})^2}$, $Ave_{VEC} = \sqrt{(U_{Backward} - U_{Forward})^2 + (V_{Backward} - V_{Forward})^2}/2.0$, and coefficients V_1 , V_1' , V_2 , and V_3 are 0.2, 0.01, 1.0, and 4.0, respectively;

$$QI_{LC} = \left[1 - \left(\tanh \left(\frac{Diff_{LC}}{\text{MAX}(L_1 * Ave_{LC}, L_1') + L_2} \right) \right)^{L_3} \right]_{All\ Bud}, \quad (10)$$

where $Diff_{LC} = \sqrt{(U_{Buddy} - U)^2 + (V_{Buddy} - V)^2}$; $Ave_{LC} = \sqrt{(U_{Buddy} + U)^2 + (V_{Buddy} + V)^2} / 2.0$; and coefficients L_1, L_1', L_2 , and L_3 are 0.2, 0.01, 1.0, and 3.0, respectively. The subscript Buddy denotes other vectors around target AMV (U, V) , which were collected. In this equation, the values in parentheses on the right-hand side are averaged over all these buddies. In addition,

$$QI_{FC} = 1 - \left(\tanh \left(\frac{Diff_{FC}}{\text{MAX}(F_1 * Ave_{FC}, F_1') + F_2} \right) \right)^{F_3}, \quad (11)$$

where $Diff_{FC} = \sqrt{(U_{Fcst} - U)^2 + (V_{Fcst} - V)^2}$; $Ave_{FC} = \frac{\sqrt{(U_{Fcst} + U)^2 + (V_{Fcst} + V)^2}}{2.0}$; coefficients F_1, F_1', F_2 , and F_3 are 0.2, 0.01, 1.0, and 3.0, respectively; and subscript Fcst denotes the collocated NWP vector (U_{Fcst}, V_{Fcst}) to the target AMV (U, V) . QI_{SPD} is the speed consistency, QI_{DIR} is the direction consistency, and QI_{VEC} is the U, V component consistency between the forward and backward vectors; QI_{LC} is the consistency between neighbors; and QI_{FC} is the consistency between the final AMVs and NWP data. The final QI is the weighted average of these five components. In addition, QI with a zero-weight value of QI_{FC} was considered. To distinguish whether this indicator depends on NWP data, it was defined as QI if the QI_{FC} weight was zero; otherwise, it was defined as QI with forecast (QIF). Similarly, the common QI (CQI) and common QI with forecast ($CQIF$) were calculated. The corresponding equations for QI, QIF, CQI , and $CQIF$ are shown in Table A2 in Appendix A. The weights used in this algorithm are presented in Table 2.

Table 2. The weights used in this algorithm for QI, QI with forecast (QIF), common QI (CQI), and CQI with forecast ($CQIF$). $W_{SPD}, W_{DIR}, W_{VEC}, W_{LC}$, and W_{FC} represent the weights of the speed, direction, vector, first-guess, and spatial consistencies, respectively.

| | W_{SPD} | W_{DIR} | W_{VEC} | W_{LC} | W_{FC} |
|--------|-----------|-----------|-----------|----------|----------|
| QI | 1 | 1 | 1 | 1 | 0 |
| QIF | 1 | 1 | 1 | 1 | 1 |
| CQI | 1 | 1 | 1 | 1 | 0 |
| $CQIF$ | 1 | 1 | 1 | 1 | 1 |

Originally developed by LeMarshall [36], the EE indicator, which is an extension of the QI , was also used as a quality flag. In our algorithm, the final AMVs were calculated with EE as well as QI , although we used only QI for quality control in this case.

3.2. Verification Methods

The AMVs can be compared with the NWP, rawinsonde, and CALIOP profiles. First, the four nearest NWP points were decided and were interpolated into the GK-2A AMV point in inverse proportions to the squared distances between the GK-2A AMV point and each NWP data point. Furthermore, all AMVs within a 150 km horizontal radius and a 25 hPa vertical distance of the rawinsonde station were collected for calculating the statistical validation scores, following the continuous glucose monitoring system criteria defined at the Third International Winds Workshop [37]. Additionally, all AMVs within 0.05° of latitude and longitude from the CLAIOP trajectory were collected.

The statistical validation scores [22], such as the mean vector difference (MVD), root-mean-square vector difference (RMSVD), bias, and root-mean-square error (RMSE), were calculated to estimate the performance of the AMVs. For the vector quantity, the vector difference (VD) between the individual wind vector (u_i, v_i) and the NWP or rawinsonde (u_r, v_r) is given by:

$$(VD)_i = \sqrt{(u_i - u_r)^2 + (v_i - v_r)^2}. \quad (12)$$

For the total number of collocated data N , the MVD is

$$MVD = \frac{1}{N} \sum_{i=1}^N (VD)_i, \quad (13)$$

and the standard deviation (SD) of the MVD is

$$SD = \sqrt{\frac{1}{N} \sum_{i=1}^N [(VD)_i - MVD]^2}. \quad (14)$$

Then, the RMSVD becomes

$$RMSVD = \sqrt{(MVD)^2 + (SD)^2}. \quad (15)$$

For scalar quantity, the speed bias is

$$BIAS = \frac{1}{N} \sum_{i=1}^N \left(\sqrt{u_i^2 + v_i^2} - \sqrt{u_r^2 + v_r^2} \right), \quad (16)$$

and the RMSE is

$$RMSE = \sqrt{\frac{1}{N} \sum_{i=1}^N \left(\sqrt{u_i^2 + v_i^2} - \sqrt{u_r^2 + v_r^2} \right)^2} \quad (17)$$

The above scores can also be normalized by the mean speed of the references, expressed as normalized MVD (NMVD), normalized RMSVD (NRMVD), normalized Bias (NBias), and normalized RMSE (NRMSE).

Additionally, we calculated the covariance and Pearson correlation coefficient to measure the relationship between the GK-2A and MTG AMVs within 0.2° of latitude and longitude. The covariance $Cov(x, y)$ between two samples x_i, y_j for a given sample size N is

$$Cov(x, y) = \frac{1}{N} \sum_{i=1}^N (x_i - \bar{x})(y_i - \bar{y}), \quad (18)$$

where $\bar{x} = \sum_{i=1}^N x_i / N$, and $\bar{y} = \sum_{i=1}^N y_i / N$. The corresponding Pearson correlation coefficient R_p is

$$R_p = \frac{Cov(x, y)}{\sigma_x \sigma_y}, \quad (19)$$

where $\sigma_x = \sqrt{\frac{1}{N} \sum_{i=1}^N (x_i - \bar{x})^2}$ and $\sigma_y = \sqrt{\frac{1}{N} \sum_{i=1}^N (y_i - \bar{y})^2}$.

4. Results

4.1. Optimization of the GK-2A AMV Algorithm

We conducted simple sensitivity tests to determine the best target box size and height assignment method in our algorithm. The AMVs were produced for July 2016 and January 2017 over the full-disk area of the AHI and were compared with the GDAPS from the KMA and rawinsonde from GTS. We removed the bad vectors by using quality control with AMVs of QIF > 80. The corresponding statistical validation scores were then calculated.

We varied the sizes from 8×8 to 48×48 for SWIR (CH07), WV (CH08), and IR (CH13) and from 16×16 to 96×96 pixels for VIS (CH03). The combined EBBT and IR/WV intercept method was used for cloudy targets, and the combined NTC and NTCC method was used for clear-air targets. We produced cloudy AMVs for CH03, 07, 08, and 13 and clear-air AMVs for CH08. As shown in

Figure 4, the mean speed of the AMVs increased as the size decreased but became slower as the size increased. Figure 5 confirms that the target box size in the smallest normalized validation scores, such as NMVD, NRMSVD, NBias, and NRMSE, was approximately 16×16 pixels for CH07, 08, and 13 and 48×48 pixels for the CH03. All scores were normalized by the speed of the corresponding references. Additionally, the best real-scale target box size was approximately 30 km regardless of the channel, as shown in Figure 4b,d. The only limitation here is that the time interval between the satellite images is fixed at 10 min, which is the smallest time gap for the AHI. However, the effect according to the time interval is clearly investigated in [20].

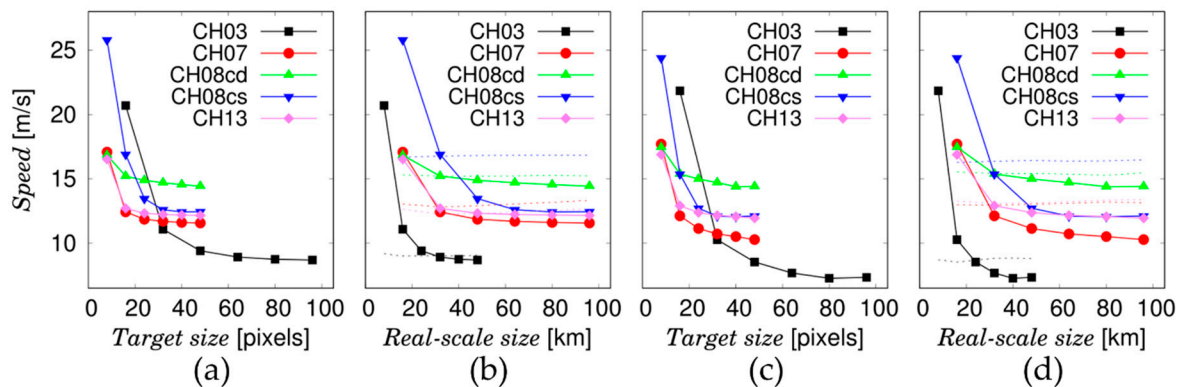


Figure 4. Plots of the mean speed of the collocated GK-2A AMVs against Global Data Assimilation and Prediction System (GDAPS) versus (a) target box size and (b) real-scale target box size for July 2016 and those against rawinsonde versus (c) target box size and (d) real-scale target box size for the same period. Each solid and dotted curve in (b) and (d) represents the mean speed of the collocated AMVs and the corresponding reference data, respectively. The results obtained for January 2016 were similar.

The CCC, EBBT, IR/WV intercept, combined EBBT and IR/WV intercept, and CO₂ slicing methods were used for cloudy targets, whereas the NTC, NTCC, and combined NTC and NTCC methods were used for clear-air targets. We produced cloudy AMVs for CH13 and clear-air AMVs for CH08 with a target box size fixed at 16×16 . All GK-2A AMVs with QIF > 80 were collected and compared with the GDAPS and rawinsonde data for July 2016 and January 2017 over the full-disk area. The results for the cloudy AMVs are shown in Tables A3 and A4 of Appendix B. For the CCC method, we used the CTP data from the GK-2A CTP retrieval algorithm. These heights showed a slow bias compared with those obtained using the other methods because they were directly affected by the quality of the CTP employed. AMVs with EBBT heights had a larger bias than AMVs with IR/WV intercept heights because heights from the former were generally lower than the reference height; EBBT works only for opaque clouds. For the IR/WV intercept method, slow bias was shown because it was valid only for semitransparent clouds; hence, it was unable to describe the heights of low, opaque clouds. Therefore, the method combining the EBBT and IR/WV intercept methods had better statistics at all levels than those obtained by using the individual methods. However, discontinuity was present because the IR/WV intercept method was valid only at heights higher than 500 hPa in this algorithm. However, the CO₂ slicing method had no discontinuity and was valid for both opaque and semitransparent cloud types. Heights from this method also had very good performances at the middle layer and best matched the reference heights among all the methods. Thus, the use of CO₂ slicing was best in our algorithm for cloudy AMVs. For clear-air AMVs, although the results for all methods were very similar, the best method was shown to be the combination of NTC and NTCC, which adopted higher heights between those from the individual methods (Tables A5 and A6 of Appendix B). This means that geostationary AMVs tend to effectively represent the flow of cloud tops.

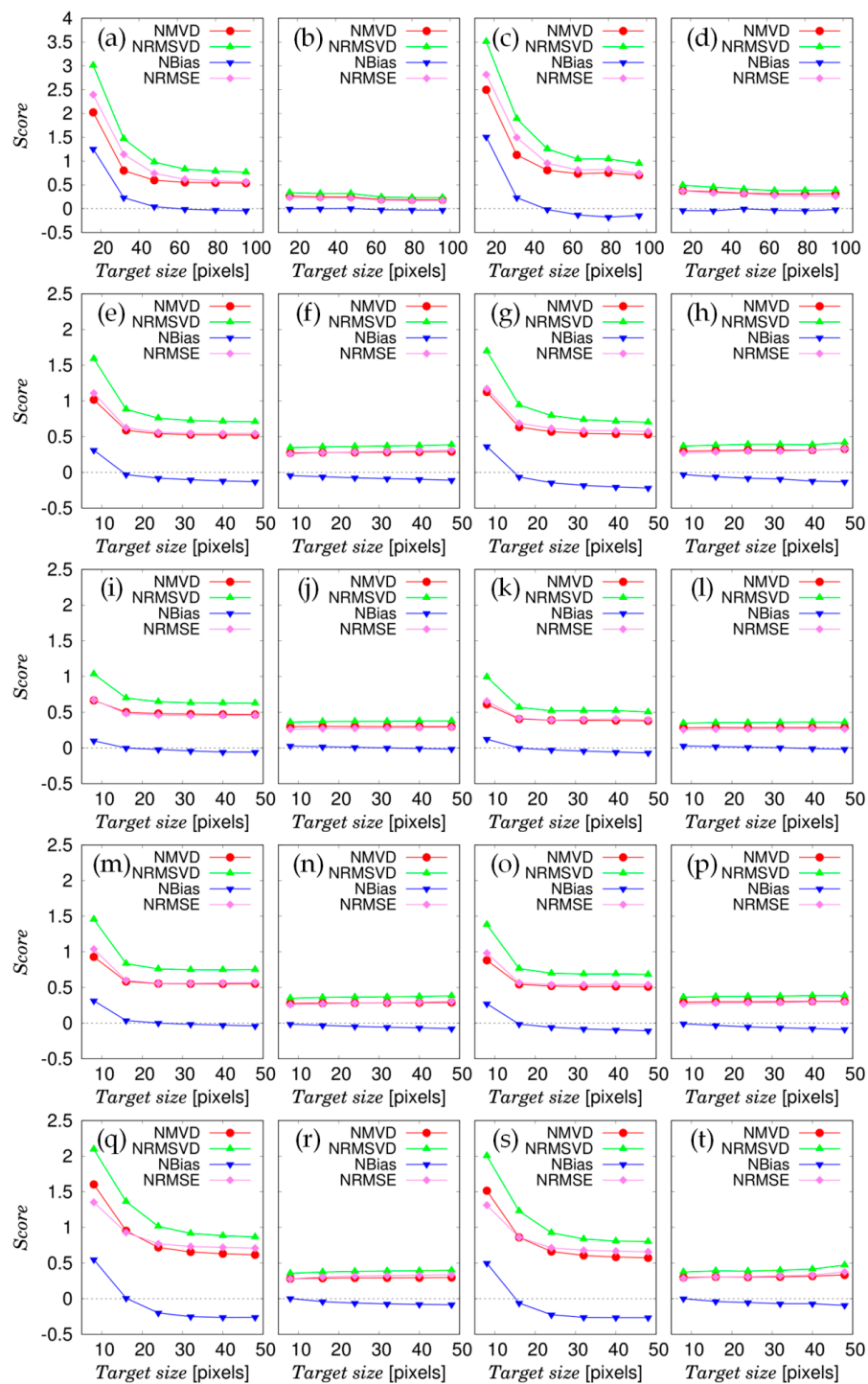


Figure 5. Plots of validation scores of normalized MVD (NMVD), normalized RMSVD (NRMSVD), normalized Bias (NBias), and normalized RMSE (NRMSE) versus the target box size for cloudy AMVs for CH03, 07, 08, and 13 and clear-air AMVs for CH08 for July 2016. All scores were normalized by the speed of the corresponding reference vectors. GK-2A AMVs for CH03 compared with GDAPS are shown for (a) nonzero QIF and (b) QIF > 80; those compared with rawinsonde are shown in (c) and (d), respectively. The same types of plots were used for cloudy AMVs for (e–h) CH07, (i–l) CH08, and (m–p) CH13 and for clear-air AMVs for (q–t) CH08. All validation scores were best at 48×48 for CH03 and at 16×16 for the other channels. Their NRMSE, NMVD, and NRMSVD became smaller than 0.5 after quality control with AMVs of QIF > 80, compared with GDAPS and rawinsonde. The results obtained for January 2017 were similar.

4.2. Comparison of GK-2A and Communication, Ocean and Meteorology Satellite (COMS) AMV Performances

The AMV retrieval algorithm was developed corresponding to the COMS satellite, which is the first-generation geostationary satellite of Korea. To objectively evaluate the performance of the GK-2A AMV algorithm, we compared the GK-2A AMVs for CH13 with the existing COMS AMVs for CH04 (10.8 μm) of MI for July 2016 and January 2017 over the ENH region. CH13 (10.45 μm) of the AHI and CH04 of the MI are IR channels that effectively represent cloud flow. We used GK-2A AMVs and COMS AMVs with a target box size of 16×16 and the combined EBBT and IR/WV intercept methods. After quality control with the AMVs of QIF > 80, the total number of GK-2A AMVs was larger than that of COMS AMVs, as shown in Table 3. The GK-2A AMVs were better than the COMS AMVs for all validation scores based on a comparison of the AMVs and GDAPS or rawinsonde at all levels. More specifically, the GK-2A AMVs were approximately 34.8% more than COMS AMVs, and the MVD, RMSVD, bias, and RMSE of the GK-2A AMVs were on average approximately 18.2% lower than those of the COMS AMVs for all periods.

Table 3. Comparison of validation scores of GK-2A and COMS AMVs with GDAPS and rawinsonde over the ENH region for July 2016 and January 2017. The GK-2A AMVs generally had better performance than COMS AMVs, considering QIF > 80.

| | GK-2A | | | | COMS | | | |
|---------------|---------------------------|---------|------------|--------|---------|---------|------------|--------|
| | GDAPS | | Rawinsonde | | GDAPS | | Rawinsonde | |
| | Jul. | Jan. | Jul. | Jan. | Jul. | Jan. | Jul. | Jan. |
| | All Levels (100–1000 hPa) | | | | | | | |
| Number | 812,874 | 766,087 | 70,163 | 61,774 | 496,981 | 549,390 | 63,573 | 49,081 |
| MVD | 3.82 | 4.45 | 4.77 | 5.44 | 5.27 | 4.88 | 5.24 | 5.81 |
| RMSVD | 4.70 | 5.88 | 5.90 | 7.15 | 7.17 | 6.50 | 6.66 | 7.38 |
| Bias | −0.01 | −0.42 | −0.47 | −1.29 | 0.69 | −0.33 | −0.56 | −1.97 |
| RMSE | 3.42 | 4.50 | 4.41 | 5.89 | 5.18 | 4.91 | 4.95 | 6.05 |
| MSPD | 12.41 | 15.88 | 15.18 | 17.96 | 13.40 | 15.91 | 16.16 | 20.59 |

Moreover, GK-2A AMVs survived more around the eye of the typhoon after quality control than COMS AMVs, in the specific case of Typhoon Nepartak at 00:00 UTC on 7 July 2016 as shown in Figure 6. These retrieved winds were compared with GDAPS and rawinsonde. The number of rawinsonde was 15, and the averaged pressure altitude of GK-2A and COMS AMVs at these stations were 236.3 (± 90.8) and 192.0 (± 41.7) hPa, respectively. The numbers in parenthesis are one sigma errors. In this case, more than 95% of both kinds of winds were above 400 hPa in the typhoon. The total number and validation scores of GK-2A AMVs were approximately 64.7% more and −18.9% lower, respectively, than COMS AMVs. The corresponding specific figures are presented in Table 4.

Table 4. Comparisons of validation scores of GK-2A and COMS AMVs with GDAPS and rawinsonde for the specific case of Typhoon Nepartak at 00:00 UTC on 7 July 2016, considering QIF > 80. GK-2A AMVs are approximately 64.7% more and 18.9% better than COMS AMV during this severe weather. The numbers in parentheses of GK-2A AMVs represent the amount of difference compared to those of COMS AMVs.

| | GK-2A | | COMS | |
|---------------|---------------|---------------|-------|-------|
| | GDAPS | Sonde | GDAPS | Sonde |
| Number | 1654 (+44.8%) | 203 (+84.6%) | 1142 | 110 |
| MVD | 5.87 (−22.6%) | 4.67 (−3.9%) | 7.58 | 4.86 |
| RMSVD | 6.86 (−27.7%) | 5.84 (−8.6%) | 9.49 | 6.39 |
| Bias | 0.30 (−76.9%) | 0.50 (+6.38%) | 1.30 | 0.47 |
| RMSE | 4.59 (−24.4%) | 4.84 (−12.8%) | 6.07 | 5.55 |
| MSPD | 15.73 | 16.36 | 16.29 | 16.86 |

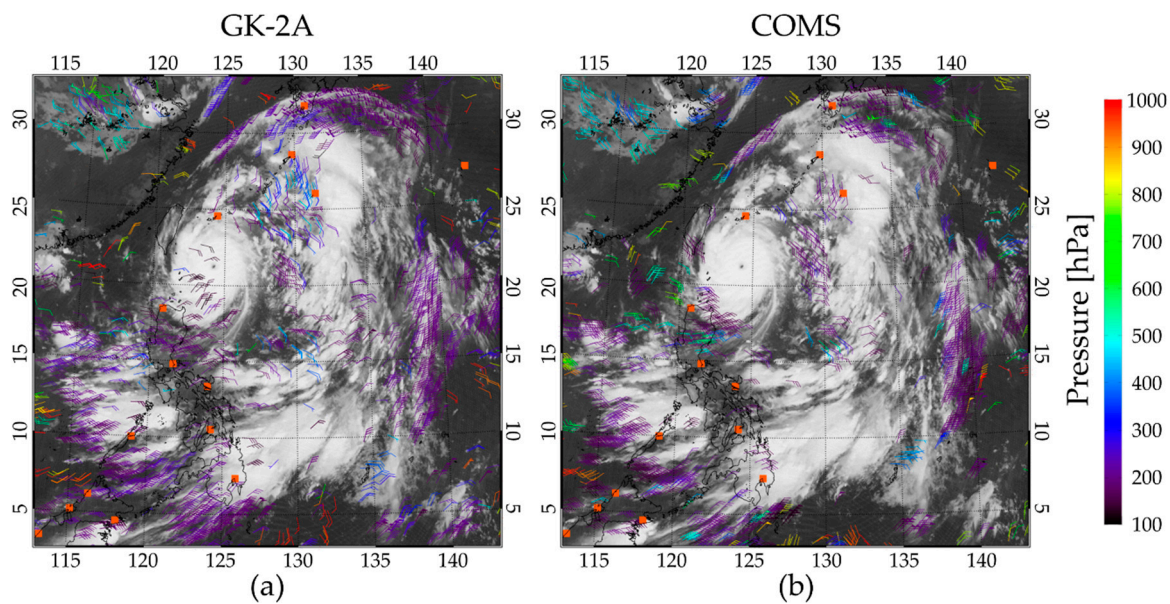


Figure 6. Plots of (a) GK-2A and (b) COMS AMVs in Typhoon Nepartak at 00:00 UTC on 7 July 2016. Colors represent pressure altitude of AMVs. The background plot is the CH13 (10.2 μm) brightness temperature of AHI. The orange square symbols represent the stations of rawinsonde captured at the same period. GK2A AMVs survived approximately 64.7% more than COMS AMVs after quality control, considering QIF > 80. Moreover, GK-2A AMVs were more consistent with GDAPS and rawinsonde than COMS AMVs. The specific figures are presented in Table 4.

4.3. Intercomparison of GK-2A and MTG AMVs

4.3.1. AMVs with CH13

The four main steps of the GK-2A AMV algorithm are based on the COMS AMV algorithm; therefore, they share many methods of the MTG AMV algorithm for geostationary data and other corrections. The similarities between the GK-2A and MTG AMVs in specific and prescribed configurations are identified in this section to verify the validity of our algorithm. Each speed, direction, height, and QI of the GK-2A and MTG AMVs with CH13 of the AHI and their performances with NWP, rawinsonde, and CALIOP profiles are compared.

First, the GK-2A AMVs in the specific and prescribed configurations were compared with the MTG AMVs in the specific and prescribed configurations. The speed and direction distributions (Figure 7a,b) of the GK-2A and MTG AMVs without quality control for CH13 of the AHI were very similar to each other. The scatter plots (Figure 7d,e) for other vectors versus the prescribed MTG AMVs of CQIF > 80 were close to the identity line with the Pearson correlation coefficients $R_p > 0.98$, and the corresponding bias/RMSE for the speed and direction were smaller than 0.1/2.5 m/s, 1.0/15.0°, respectively. Especially, the corresponding bias/RMSE for the speed and direction in the prescribed GK-2A and MTG AMVs were $-0.07/2.19$ m/s and $0.21/14.8^\circ$, respectively. These results were expected because the target selection and tracking processes of these two algorithms were very similar.

As shown in Figure 7c, the height distributions of the GK-2A and MTG AMVs without quality control in the prescribed configuration were very similar. In the corresponding scatter plots of Figure 7f, the Pearson correlation coefficients R_p between the prescribed GK-2A and MTG AMVs of CQIF > 80 were 0.97. The corresponding bias/RMSE for the heights was 2.61/62.9 hPa. This result was also expected because they all used the same cloud information from NOAA/NESDIS. For the GK-2A AMVs in the specific configuration, the CCC heights using the GK-2A CTP were more assigned at about 150 hPa; those from the EBBT and IR/WV intercept method were about 450 hPa; and those from CO₂ slicing were about 950 hPa. These values were compared to the MTG AMVs of heights from the NOAA/NESDISS in the prescribed configuration. The corresponding validation scores are in Table 5,

with NWP and rawinsonde *U* and *V* profiles. The GK-2A AMVs with heights from the CO₂ slicing method or the combined EBBT and IR/WV intercept methods in the specific configuration showed positive bias, whereas the GK-2A AMVs with heights from the CCC method in the specific configuration showed negative bias. The MVD, RMSVD, bias and RMSE for GK-2A AMVs with heights obtained from the CO₂ slicing method were the lowest among all specific GK-2A AMV heights. Moreover, the validation scores between the GK-2A AMVs with heights in the prescribed configuration and reference profiles were very similar to those of the MTG AMVs in the both specific and prescribed configurations.

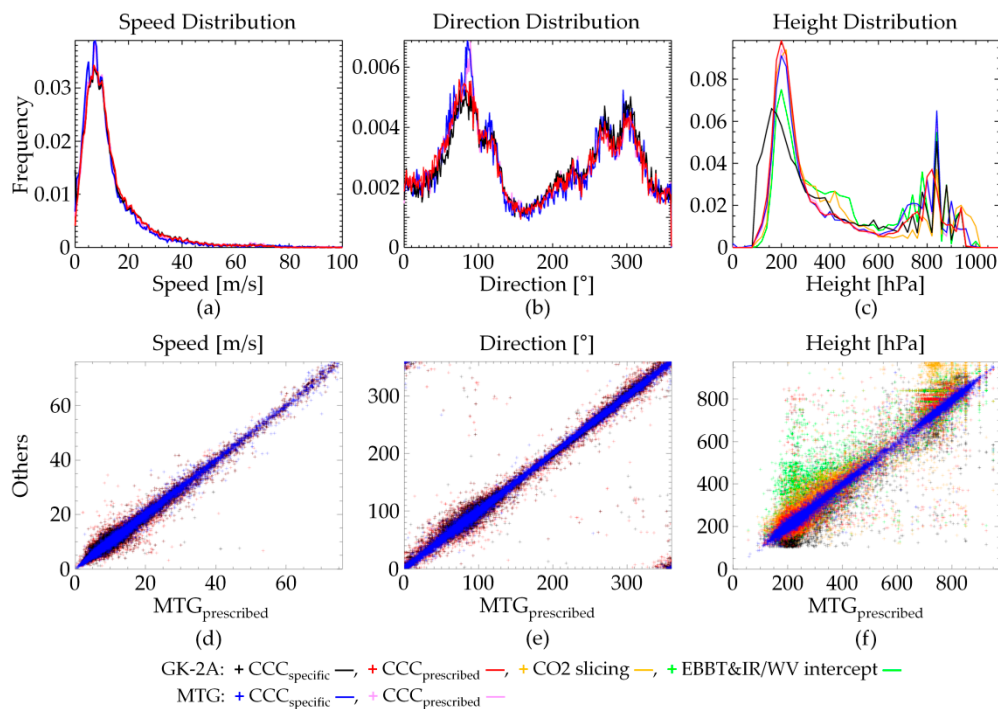


Figure 7. Distribution comparison of (a) speed, (b) direction, and (c) height of GK-2A and MTG AMVs for 12:10 UTC on 21 July 2016. (a), (b) GK-2A AMVs with heights from CCC in the specific configuration (black) and in the prescribed configuration (red) as well as MTG AMVs with heights from CCC in the specific configuration (blue) and in the prescribed configuration (violet). The GK-2A AMVs with heights obtained from the CO₂ slicing (orange) and the combined use of EBBT and IR/WV intercept methods (green) are additionally shown in (c). (d–f) the corresponding scatter plots are shown for the collocated AMVs for others versus MTG AMVs with heights from CCC in the prescribed configuration. The colors are the same as those in (a–c). The results for 05:40 UTC on 21 July 2016 were very similar.

Table 5. Validation scores of GK-2A and MTG AMVs compared with GDAPS, rawinsonde in the specific configuration, and ECMWF and rawinsonde in the prescribed configuration for both 05:40 and 12:10 UTC on 21 July 2016. AMVs with CQIF > 80 were collected.

| | GK-2A | | | | | | | | MTG | | | |
|---------------|------------|-------|-------------------------|-------|------------|-------|--------|-------|----------|-------|------------|-------|
| | Specific | | | | Prescribed | | | | Specific | | Prescribed | |
| | EBBT&IR/WV | | CO ₂ Slicing | | CCC | | CCC | | CCC | | CCC | |
| | NWP | Sonde | NWP | Sonde | NWP | Sonde | NWP | Sonde | NWP | Sonde | NWP | Sonde |
| Number | 75,963 | 2027 | 78,581 | 2356 | 73,252 | 1981 | 84,469 | 2800 | 43,845 | 1309 | 86,460 | 2957 |
| MVD | 5.44 | 5.86 | 5.44 | 5.70 | 5.67 | 7.02 | 4.44 | 5.80 | 4.35 | 5.67 | 4.54 | 5.76 |
| RMSVD | 7.53 | 8.19 | 7.35 | 7.69 | 7.64 | 8.66 | 5.98 | 7.64 | 5.87 | 7.29 | 6.19 | 7.52 |
| Bias | 0.58 | 0.59 | 0.07 | 0.33 | −0.89 | −0.93 | −0.26 | −0.45 | −0.31 | −0.59 | −0.14 | −0.43 |
| RMSE | 5.62 | 6.03 | 5.49 | 5.37 | 5.79 | 6.66 | 4.58 | 5.35 | 4.47 | 5.13 | 4.70 | 5.31 |
| MSPD | 14.39 | 13.62 | 14.71 | 14.07 | 14.41 | 15.59 | 14.51 | 14.66 | 13.96 | 14.84 | 13.92 | 14.13 |

The processes used to estimate the QI values in the GK-2A and MTG AMV algorithms differed from each other, as shown in Table A2 in Appendix A. The QI distributions of GK-2A were, thus, different from those of MTG. Moreover, significant differences were shown in the spatial consistency component. The GK-2A AMVs collected all buddies existing within the given elliptical radius around the reference vector to calculate the final spatial consistency, whereas the MTG AMVs collected only two buddies with the best spatial consistency. Thus, more vectors with a large QI and QIF were obtained among the MTG AMVs than those among the GK-2A AMVs. However, the CQI and CQIF distributions were very similar because the two algorithms used the same module to calculate the CQI and CQIF, as shown in Figure 8.

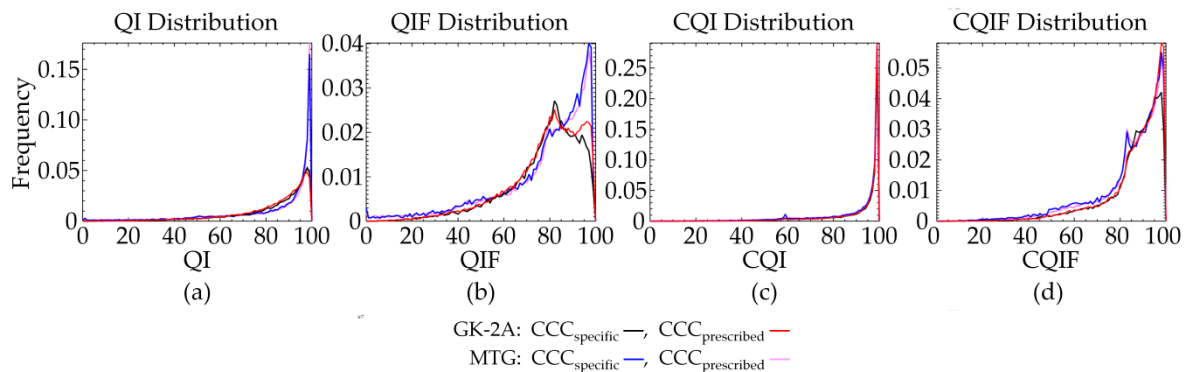


Figure 8. Distribution comparisons of (a) QI, (b) QIF, (c) CQI, and (d) CQIF of GK-2A and MTG AMVs for 12:10 UTC on 21 July 2016. The colors represent GK-2A AMVs with heights from CCC in the specific configuration (**black**) and CCC in prescribed configuration (**red**) as well as MTG AMVs with heights from the CCC in specific configuration (**blue**) and CCC in the prescribed configuration (**violet**). The results obtained for 05:40 UTC on 21 July 2016 were very similar.

According to the speed, direction, height, and QI distribution, strong agreement was confirmed between the GK-2A and MTG AMVs in the prescribed configuration. This proves that the GK-2A AMV retrieval algorithm works properly. Finally, the GK-2A and MTG AMVs were compared with the CALIOP lidar data, considering $QIF > 80$. The GK-2A and MTG AMVs heights from CCC in the prescribed configuration and the additional GK-2A AMV heights from CO₂ slicing and the combined EBBT and IR/WV intercept methods in the specific configuration, were collocated against the track of CALIOP. They were all shown to be consistent with the CALIOP level 1 and level 2 profiles obtained for 05:40 UTC in July 2016, as shown in Figure 9.

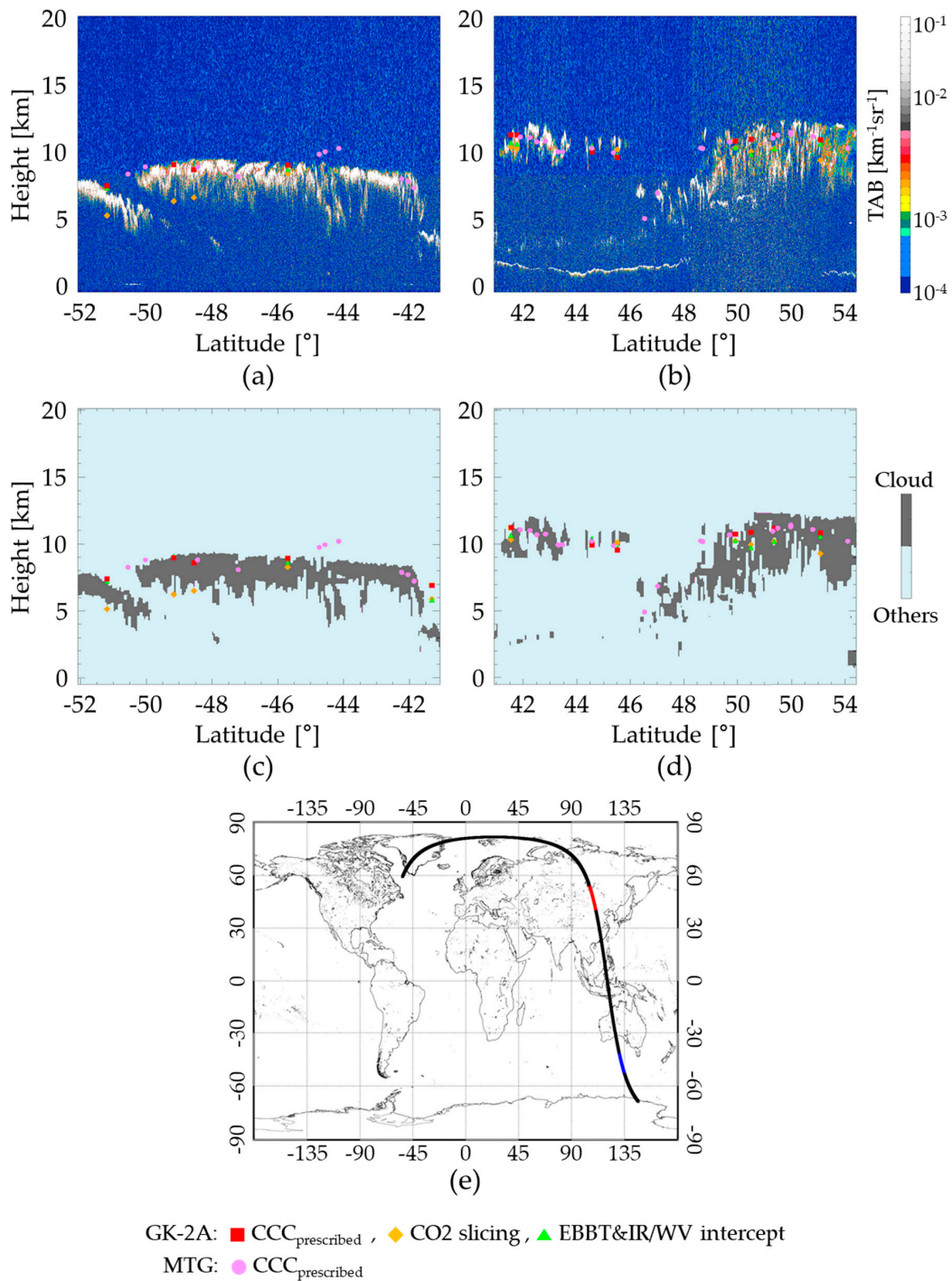


Figure 9. Comparison of AMV heights and Cloud-Aerosol Lidar with Orthogonal Polarization (CALIOP) level 1 and 2 lidar products for 05:40 UTC on 21 July 2016. (a) CALIOP 532 total attenuated backscatter (TAB) and (c) level 2 cloud profiles for the red segment of (e). (b) CALIOP 532 attenuated backscatter and (d) level 2 cloud profiles for the blue segment of (e). Symbols represent prescribed CCC heights (●) of MTG AMVs and the prescribed CCC heights (■), specific CO₂ slicing heights (◆), and EBBT and IR/WV intercept heights (▲) of GK-2A AMVs, respectively. (e) The corresponding track of CALIOP is also plotted. No collocated AMV data were available for 12:10 UTC on 21 July 2016.

4.3.2. AMVs with CH03, 07, 08, and 10

For a cloudy target, additional GK-2A and MTG AMVs for CH03, 07, 08, and 10 in the prescribed configuration were simply compared with each other for 05:40 and 12:10 UTC on 21 July 2016. As shown

in Section 4.3.1, the Pearson correlation coefficient R_P of the speed, direction, and height distribution of the GK-2A and MTG AMVs were larger than 0.95. The corresponding bias/RMSE for the speed, direction, and height were smaller than 0.1/2.5 m/s, 1.0/15.0°, and 5.0/70.0 hPa, respectively, considering CQIF > 80. This similarity cannot guarantee that the quality of GK-2A AMVs is objectively high. However, the bias/RMSE and MVD/RMSVD compared with ECMWF and rawinsonde was smaller than 1.0/6.0 and 7.0/8.0 m/s for all cases, and these met the Geostationary Operational Environmental Satellite-R (GOES-R) requirements [10]. Results are based on only two samples of the datasets on 21 July 2016 in Tables 6 and 7.

Table 6. Validation scores of GK-2A AMVs compared with ECMWF and rawinsonde profiles in the prescribed configuration for both 05:40 and 12:10 UTC on 21 July 2016. All AMVs with CQIF > 80 were collected.

| | 03 | | 07 | | 08 | | 10 | |
|---------------|--------|-------|--------|-------|--------|-------|--------|-------|
| | NWP | Sonde | NWP | Sonde | NWP | Sonde | NWP | Sonde |
| Number | 35,506 | 156 | 39,692 | 2018 | 51,787 | 2686 | 59,474 | 2945 |
| MVD | 4.45 | 6.52 | 4.24 | 5.71 | 5.28 | 5.90 | 5.15 | 5.97 |
| RMSVD | 6.08 | 7.38 | 5.89 | 7.68 | 6.80 | 7.76 | 6.68 | 7.80 |
| Bias | −0.56 | −0.37 | −0.76 | −0.80 | 0.37 | 0.21 | 0.30 | −0.02 |
| RMSE | 4.38 | 5.48 | 4.54 | 5.48 | 5.20 | 5.32 | 5.13 | 5.46 |
| MSPD | 12.24 | 14.12 | 13.88 | 13.49 | 15.72 | 15.77 | 16.92 | 16.33 |

Table 7. Validation scores of MTG AMVs compared with ECMWF and rawinsonde profiles in the prescribed configuration for both 05:40 and 12:10 UTC on 21 July 2016. All AMVs with CQIF > 80 were collected. Results are very similar to those of GK-2A AMVs in Table 6.

| | 03 | | 07 | | 08 | | 10 | |
|---------------|--------|-------|--------|-------|--------|-------|--------|-------|
| | NWP | Sonde | NWP | Sonde | NWP | Sonde | NWP | Sonde |
| Number | 39,127 | 89 | 36,939 | 1706 | 54,775 | 2867 | 55,761 | 2939 |
| MVD | 4.47 | 6.24 | 4.28 | 5.75 | 5.47 | 6.27 | 5.28 | 5.88 |
| RMSVD | 6.11 | 7.17 | 5.87 | 7.75 | 6.84 | 8.16 | 6.62 | 7.95 |
| Bias | −0.75 | −0.71 | −0.67 | −0.89 | 0.95 | 0.97 | 0.62 | 0.52 |
| RMSE | 4.28 | 5.02 | 4.39 | 5.42 | 5.19 | 5.89 | 5.00 | 5.58 |
| MSPD | 11.13 | 13.46 | 13.14 | 13.35 | 15.48 | 16.38 | 14.97 | 15.35 |

5. Discussion

5.1. Validation and Optimization of the GK-2A AMV Algorithm

Simple sensitivity tests of the target box sizes and height assignment methods were performed. A smaller target box size was shown to correspond to faster speeds, and a larger target box size decreased the speed without quality control. This means that it is difficult to track the target when the target box sizes are excessively small or large. These results are in good agreement with those reported in previous research [19,20,38]. However, the validation scores with AMVs of QIF > 80 were almost independent of the target box size regardless of the channel. We found the best target sizes to be 16 × 16 for CH07, 08, and 13 channels and 48 × 48 for CH 03. This indicates that 24–32 km of the target box in the real-scale distance is best for tracking the target regardless of the spatial resolution for the channels. Regarding the height assignment method for cloudy targets, the CCC method is strongly dependent on the quality of the CTP data used; hence, it is not suitable for application in the GK-2A AMV algorithm because the GK-2A CTP algorithm is yet to be developed. However, we strongly expect that this method will show very good performance if the CTP data used has high quality [30]. The combined use of the EBBT and IR/WV intercept methods showed better statistics at all levels than those shown by the individual methods because the EBBT method is used only for opaque clouds, and the IR/WV intercept method only applies for semitransparent clouds [7,24,27]. CO₂ slicing was shown to be the best method for cloudy targets as presented in Tables A3 and A4 in Appendix B. This was valid for both the opaque and semitransparent clouds [28,29]. For clear-air targets, the combined use of NTC and NTCC methods produced heights with the best validation scores. Moreover, it was confirmed that

these GK-2A AMVs were more and better than those of COMS AMVs with the same target box size. In the specific case of Typhoon Nepartak in July 2016, GK-2A AMVs survived approximately 64.7% more than COMS AMVs after quality control, considering $QIF > 80$. The corresponding validation scores with GDAPS and rawinsonde were approximately 18.9% lower than those of COMS AMVs. It means that GK-2A AMV algorithms could track the target better than those of COMS even though there was severe weather.

5.2. Intercomparisons of GK-2A and MTG AMVs

In the prescribed configuration, all conditions for calculating the GK-2A and MTG AMVs were exactly the same. A comparison of the GK-2A and MTG AMVs with CH03, 07, 08, and 10 for the cloudy targets revealed strong similarity between them for all channels. This proves that the GK-2A AMV algorithms work properly because the retrieval processes of these two algorithms are very similar. In the specific configuration, each algorithm uses its own input data with different target box sizes and height assignment methods. In this case, the heights of the GK-2A AMVs differed slightly from those of the MTG AMVs; however, the validation results with NWP and rawinsonde data are reasonable, even though only two datasets for each AMV were used. All the corresponding validation scores met GOES-R requirements [10]. Moreover, all GK-2A AMV heights and MTG heights with CH13 were consistent with the CALIOP data. These results provide further objective evidence that the GK-2A AMV algorithms were successfully derived.

5.3. Novelty and Limitations

The AHI data of the Himawari-8 have higher spatial and temporal resolutions than those obtained from MI of COMS. Thus, the GK-2A AMV algorithm uses more channels than the COMS AMV algorithm. In this algorithm, the GK-2A AMVs were derived for one VIS channel, one SWIR channel, three WV channels, and two IR channels of the AHI, compared with the COMS AMVs using only one of each individual VIS, SWIR, WV, and IR channel. The additional CO₂ channel, which was not used in the MI of the COMS, was used to assign the heights of wind. In addition, with the advanced spatial and temporal resolution, the GK-2A AMV algorithm derived additional vectors with higher quality than those of the COMS AMV algorithm over the same area. Therefore, the improved Korean geostationary AMV algorithm, as detailed in this study, is confirmed to be superior. Finally, the similarity between the GK-2A and MTG AMVs was also confirmed through reasonable validation scores.

However, our validation periods covered only July 2016 and January 2017. Thus, our main results could be dependent on these periods. Additionally, the performance of the GK-2A AMV is strongly influenced by the quality of the CLD and CTP; however, neither the GK-2A CLD nor CTP retrieval algorithms have been developed. We confirmed that the AMVs with CLD and CTP information from the NOAA/NESDIS have reasonable validation scores with NWP and rawinsonde profiles, as shown in Section 4.3. Thus, we strongly expect the CCC method to become the best height assignment method, provided high-quality cloud information is used.

6. Conclusions

By using Himawari-8/AHI data, we developed an AMV algorithm for the GK-2A satellite, which launched in 2018. This study is significant because it enabled us to clearly describe our algorithm and to prove its validity. We evaluated the performance of the GK-2A AMV algorithm by varying the target sizes and height assignment methods for each type of AMV and comparing the GK-2A AMVs with rawinsonde and GDAPS data obtained in July 2016 and January 2017. The best target box size was shown to be 16×16 pixels for CH07, 08, and 13 and 48×48 pixels for CH03. The best height assignment method was the CO₂ slicing method for cloudy targets and the combined method of NTC and NTCC for clear-air targets. We also confirmed that the GK-2A AMVs more accurately described severe weather, like a typhoon, and generally performed better than the COMS AMVs with the same target box size. Finally, strong similarity was verified between the GK-2A and MTG AMVs by using

the AHI of Himawari-8 for two datasets for each AMV recorded on 21 July 2016. The results proved that the GK-2A AMV retrieval algorithms were derived successfully. This study provides significant information for optimizing the performance of the GK-2A AMVs when AMI data are applied to this algorithm because the properties of the AMI are similar to those of the AHI. Moreover, our research findings provide a basis for advancing AMV retrievals in the future based on the high spatial and temporal resolutions of geostationary satellite data.

Author Contributions: Conceptualization, methodology, software, and validation: S.M.O.; resources and investigation: S.M.O., M.C., R.B., and I.-C.S.; writing—original draft preparation: S.M.O.; writing—review and editing: S.M.O. and I.-C.S.; supervision: I.-C.S.

Funding: This work was funded by the National Meteorological Satellite Centre (NMSC) of the Korea Meteorological Administration (KMA) through Grant No. 153-3100-3137-305-210-13.

Acknowledgments: I (S. M. Oh) thank my colleagues I. C. Shin (NMSC), R. B. Borde (EUM), and M. Carranza (EUM) for their cooperation. The authors would like to thank the anonymous reviewers for their valuable comments.

Conflicts of Interest: The authors declare no conflict of interest.

Appendix A. Differences between GK-2A and MTG AMV Algorithms

The GK-2A AMV algorithm is described in Section 3.1. In this section, we compare the GK-2A AMV algorithm with the MTG AMV algorithms. The MTG AMV algorithms proceed in the order of target selection, tracking, height assignment, and quality control. However, the GK-2A AMV algorithm proceeds in the order of target selection, height assignment, tracking, and quality control, considering the possibility that the height information of the AMVs is used. These two algorithms use optimal methods for target selection and the CC method for tracking. For cloudy targets, both algorithms assign the height using the CCC method in the height-assignment process. The GK-2A AMV algorithm uses an additional height assignment method for cloudy targets, such as EBBT, IR/WV intercept, or CO₂ slicing. For clear-air targets, both algorithms use the NTC and NTCC methods in the height assignment process. The MTG AMV algorithm also uses the EBBT method for clear-air targets. A summary of these differences is listed in Table A1.

During the quality control process, quality flags are calculated for each vector. The GK-2A AMV algorithm uses both QI and EE, whereas the MTG AMV algorithm uses QI as a quality flag. In GK-2A QI algorithm, the final QI flags are the weighted averages of five components: speed consistency QI_{SPD} , direction consistency QI_{DIR} , vector consistency QI_{VEC} between the backward and forward vectors, first-guess consistency QI_{FC} between the final AMV and the first-guess vector, and spatial consistency QI_{LC} between the final AMV and the surrounding vectors. However, the weighted average of these five QI components, multiplied the additional height consistency described in [35], becomes the final QI value in MTG QI algorithm. Moreover, CQI and CQIF are also used because there is a better agreement between GK-2A and MTG AMVs. Further details are shown in Table A2.

Table A1. Comparison of characteristics of GK-2A and MTG AMV algorithms.

| | GK-2A AMV | MTG AMV |
|--------------------------|--|---|
| Target box size | VIS: 48 by 48 Others: 16 by 16 | 16 by 16 (24 by 24) |
| Target center | Pixels with the largest standard deviation | Pixels with the largest standard deviation |
| Grid step size | Same with target box size | Same with target box size |
| Search box size | VIS: 201 by 201 Others: 54 by 54 | 54 by 54 (80 by 80) |
| Tracking | CC | CC |
| Height assignment | Cloudy target: CCC, EBBT, IR/WV intercept, and CO ₂ slicing Clear-air target: NTC and NTCC | Cloudy target: CCC Clear-air target: NTC, NTCC, and EBBT |
| Quality Control | QI, EE | QI |

Table A2. Comparisons of GK-2A QI, MTG QI, and common QI. The final QI flags are the weighted averages of five components including speed consistency QI_{SPD} , direction consistency QI_{DIR} , and vector consistency QI_{VEC} , first-guess consistency QI_{FC} , and the spatial consistency QI_{LC} in GK-2A and common QI algorithms. However, the weighted average of these five QI components, multiplied the additional height consistency, becomes the final QI value in MTG QI algorithm.

| | GK-2A QI | MTG QI | Common QI |
|------------|--|--|--|
| QI_{SPD} | $1 - \left(\tanh \left(\frac{ Diff_{SPD} }{MAX(S_1 * Vel_{SPD}, S_1') + S_2} \right) \right)^{S_3}$ $Diff_{SPD} = SPD_{Backward} - SPD_{Forward}$ $Vel_{SPD} = (SPD_{Backward} + SPD_{Forward}) / 2.0$ $S_1 = 0.2, S_1' = 0.01, S_2 = 1.0, \text{ and } S_3 = 2.5$ $W_{SPD} = 1.0$ | $1 - \left(\tanh \left(\frac{ Diff_{SPD} }{MAX(S_1 * Vel_{SPD}, S_1') + S_2} \right) \right)^{S_3}$ $Diff_{SPD} = SPD_{Backward} - SPD_{Forward}$ $Vel_{SPD} = (SPD_{Backward} + SPD_{Forward}) / 2.0$ $S_1 = 0.2, S_1' = 0.01, S_2 = 1.0, \text{ and } S_3 = 3.0$ $W_{SPD} = 0.0$ | $1 - \left(\tanh \left(\frac{ Diff_{SPD} }{S_1 * Vel_{SD} + S_2} \right) \right)^{S_3}$ $Diff_{SPD} = SPD_{Backward} - SPD_{Forward}$ $Vel_{SPD} = (SPD_{Backward} + SPD_{Forward}) / 2.0$ $S_1 = 0.2, S_2 = 1.0, \text{ and } S_3 = 3.0$ $W_{SPD} = 1.0$ |
| QI_{DIR} | $1 - \left(\tanh \left(\frac{ Diff_{DIR} }{D_1 * \exp \left(-\frac{Vel_{DIR}}{D_2} \right) + D_2'} \right) \right)^{D_3}$ $Diff_{DIR} = DIR_{Backward} - DIR_{Forward}$ $Vel_{DIR} = (SPD_{Backward} + SPD_{Forward}) / 2.0$ $D_1 = 20.0, D_2 = 10.0, D_2' = 10.0, \text{ and } D_3 = 4.0$ $W_{DIR} = 1.0$ | $1 - \left(\tanh \left(\frac{ Diff_{DIR} }{D_1 * \exp \left(-\frac{Vel_{DIR}}{D_2} \right) + D_1' * Vel_{DIR} + D_2'} \right) \right)^{D_3}$ $Diff_{DIR} = DIR_{Backward} - DIR_{Forward}$ $Vel_{DIR} = (SPD_{Backward} + SPD_{Forward}) / 2.0$ $D_1 = 20.0, D_2 = 10.0, D_1' = 0.0, D_2' = 10.0, \text{ and } D_3 = 4.0$ $W_{DIR} = 0.0$ | $1 - \left(\tanh \left(\frac{ Diff_{DIR} }{D_1 * \exp \left(-\frac{Vel_{DIR}}{D_2} \right) + D_2'} \right) \right)^{D_3}$ $Diff_{DIR} = DIR_{Backward} - DIR_{Forward}$ $Vel_{DIR} = (SPD_{Backward} + SPD_{Forward}) / 2.0$ $D_1 = 20.0, D_2 = 10.0, D_2' = 10.0, \text{ and } D_3 = 4.0$ $W_{DIR} = 1.0$ |
| QI_{VEC} | $1 - \left(\tanh \left(\frac{Diff_{VEC}}{MAX(V_1 * Ave_{VEC}, V_1') + V_2} \right) \right)^{V_3}$ $Diff_{VEC} = \sqrt{(U_{Back} - U_{For})^2 + (V_{Back} - V_{For})^2}$ $Ave_{VEC} = \sqrt{(U_{Back} - U_{For})^2 + (V_{Back} - V_{For})^2} / 2.0$ $V_1 = 0.2, V_1' = 0.01, V_2 = 1.0, \text{ and } V_3 = 4.0$ $W_{VEC} = 1.0$ | $1 - \left(\tanh \left(\frac{Diff_{VEC}}{MAX(V_1 * Ave_{VEC}, V_1') + V_2} \right) \right)^{V_3}$ $Diff_{VEC} = \sqrt{(U_{Back} - U_{For})^2 + (V_{Back} - V_{For})^2}$ $Ave_{VEC} = \sqrt{(U_{Back} - U_{For})^2 + (V_{Back} - V_{For})^2} / 2.0$ $V_1 = 0.2, V_1' = 0.01, V_2 = 1.0, \text{ and } V_3 = 3.0$ $W_{VEC} = 2.0$ | $1 - \left(\tanh \left(\frac{Diff_{VEC}}{V_1 * Vel_{VEC} + V_2} \right) \right)^{V_3}$ $Diff_{VEC} = \sqrt{(U_{Back} - U_{For})^2 + (V_{Back} - V_{For})^2}$ $Vel_{VEC} = (SPD_{Backward} + SPD_{Forward}) / 2.0$ $V_1 = 0.2, V_2 = 1.0, \text{ and } V_3 = 3.0$ $W_{VEC} = 1.0$ |
| QI_{LC} | $\left[1 - \left(\tanh \left(\frac{Diff_{LC}}{MAX(L_1 * Ave_{LC}, L_1') + L_2} \right) \right)^{L_3} \right]_{All\ Bud}$ $Diff_{LC} = \sqrt{(U_{Buddy} - U)^2 + (V_{Buddy} - V)^2}$ $Ave_{LC} = \sqrt{(U_{Buddy} + U)^2 + (V_{Buddy} + V)^2} / 2.0$ $L_1 = 0.2, L_1' = 0.01, L_2 = 1.0, \text{ and } L_3 = 3.0$ $W_{LC} = 2.0$ | $\left[1 - \left(\tanh \left(\frac{Diff_{LC}}{MAX(L_1 * Ave_{LC}, L_1') + L_2} \right) \right)^{L_3} \right]_{Best\ Bud}$ $Diff_{LC} = \sqrt{(U_{Buddy} - U)^2 + (V_{Buddy} - V)^2}$ $Ave_{LC} = \sqrt{(U_{Buddy} + U)^2 + (V_{Buddy} + V)^2} / 2.0$ $L_1 = 0.2, L_1' = 0.01, L_2 = 1.0, \text{ and } L_3 = 3.0$ $W_{LC} = 2.0$ | $\left[1 - \left(\tanh \left(\frac{Diff_{LC}}{L_1 * Ave_{LC} + L_2} \right) \right)^{L_3} \right]_{Best\ Bud}$ $Diff_{LC} = \sqrt{(U_{Buddy} - U)^2 + (V_{Buddy} - V)^2}$ $Ave_{LC} = \sqrt{(U_{Buddy} + U)^2 + (V_{Buddy} + V)^2} / 2.0$ $L_1 = 0.2, L_2 = 1.0, \text{ and } L_3 = 3.0$ $W_{LC} = 2.0$ |
| QI_{FC} | $1 - \left(\tanh \left(\frac{Diff_{FC}}{MAX(F_1 * Ave_{FC}, F_1') + F_2} \right) \right)^{F_3}$ $Diff_{FC} = \sqrt{(U_{Fcst} - U)^2 + (V_{Fcst} - V)^2}$ $Ave_{FC} = \sqrt{(U_{Fcst} + U)^2 + (V_{Fcst} + V)^2} / 2.0$ $F_1 = 0.2, F_1' = 0.01, F_2 = 1.0, \text{ and } F_3 = 3.0$ $W_{FC} = 0.0 \text{ for } QI \text{ (} W_{FC} = 1.0 \text{ for } QIF)$ | $1 - \left(\tanh \left(\frac{Diff_{FC}}{MAX(F_1 * Ave_{FC}, F_1') + F_2} \right) \right)^{F_3}$ $Diff_{FC} = \sqrt{(U_{Fcst} - U)^2 + (V_{Fcst} - V)^2}$ $Ave_{FC} = \sqrt{(U_{Fcst} + U)^2 + (V_{Fcst} + V)^2} / 2.0$ $F_1 = 0.4, F_1' = 0.01, F_2 = 1.0, \text{ and } F_3 = 2.0$ $W_{FC} = 0.0 \text{ for } QI \text{ (} W_{FC} = 1.0 \text{ for } QIF)$ | $1 - \left(\tanh \left(\frac{Diff_{FC}}{F_1 * Ave_{FC} + F_2} \right) \right)^{F_3}$ $Diff_{FC} = \sqrt{(U_{Fcst} - U)^2 + (V_{Fcst} - V)^2}$ $Ave_{FC} = \sqrt{U_{Fcst}^2 + V_{Fcst}^2}$ $F_1 = 0.4, F_2 = 1.0, \text{ and } F_3 = 2.0$ $W_{FC} = 0.0 \text{ for } CQI \text{ (} W_{FC} = 1.0 \text{ for } CQIF)$ |

Appendix B. Performance according to Height Assignment Methods of GK-2A AMV Algorithm

Sensitivity tests about height assignments of the GK-2A AMV algorithm are conducted. The CCC, EBBT, IR/WV intercept, combined EBBT and IR/WV intercept, and CO₂ slicing methods were used for cloudy targets, whereas the NTC, NTCC, and combined NTC and NTCC methods were used for clear-air targets. We produced cloudy AMVs for CH13 and clear-air AMVs for CH08 with a target box size fixed at 16 × 16. All GK-2A AMVs with QIF > 80 were collected and compared with the GDAPS and rawinsonde data for July 2016 and January 2017 over the full-disk area. In Tables A3–A6, the best scores are in bold and the worst scores are in italics.

Table A3. Comparisons between GK-2A cloudy AMVs for CH13 and GDAPS over the full-disk area for July 2016 and January 2017. The CCC, EBBT, IR/WV intercept, CO₂ slicing methods, and the combination of EBBT and IR/WV intercept methods were used for producing GK-2A AMVs, considering QIF > 80. The best scores are in bold and the worst scores are in italics. CO₂ slicing method is best on average at all levels.

| | CCC | | EBBT&IR/WV | | EBBT | | IR/WV | | CO ₂ | |
|-----------------------------|-------------|-------------|------------|-----------|-----------|-------------|---------|---------|-----------------|-------------|
| | Jul. | Jan. | Jul. | Jan. | Jul. | Jan. | Jul. | Jan. | Jul. | Jan. |
| All levels (100–1000 hPa) | | | | | | | | | | |
| Number | 1,486,672 | 1,326,612 | 1,449,203 | 1,254,004 | 1,325,452 | 1,115,233 | 678,284 | 628,372 | 1,357,057 | 1,244,000 |
| MVD | 4.94 | 5.27 | 4.14 | 4.37 | 4.27 | 4.52 | 4.94 | 4.88 | 4.12 | 4.29 |
| RMSVD | 6.56 | 7.23 | 5.41 | 5.76 | 5.59 | 5.91 | 6.20 | 6.31 | 5.23 | 5.48 |
| Bias | −0.71 | −0.85 | 0.33 | 0.31 | 0.55 | 0.62 | 0.24 | 0.20 | −0.07 | 0.07 |
| RMSE | 5.23 | 5.98 | 4.06 | 4.38 | 4.19 | 4.44 | 4.64 | 4.69 | 3.91 | 4.07 |
| MSPD | 15.49 | 17.17 | 15.32 | 16.42 | 15.39 | 16.43 | 17.71 | 18.49 | 16.32 | 16.87 |
| High levels (100–400 hPa) | | | | | | | | | | |
| Number | 840,674 | 747,401 | 734,148 | 672,608 | 532,274 | 484,144 | 678,284 | 628,372 | 786,885 | 709,679 |
| MVD | 5.93 | 6.10 | 4.83 | 4.78 | 5.29 | 5.12 | 4.94 | 4.88 | 4.57 | 4.63 |
| RMSVD | 7.47 | 8.12 | 6.05 | 6.19 | 6.56 | 6.54 | 6.20 | 6.31 | 5.61 | 5.79 |
| Bias | −1.40 | −1.77 | 0.24 | 0.19 | 0.34 | 0.55 | 0.24 | 0.20 | −0.07 | −0.08 |
| RMSE | 5.94 | 6.69 | 4.53 | 4.61 | 4.88 | 4.71 | 4.64 | 4.69 | 4.15 | 4.21 |
| MSPD | 17.68 | 19.13 | 17.44 | 18.07 | 18.49 | 18.69 | 17.71 | 18.49 | 17.87 | 18.02 |
| Middle levels (400–700 hPa) | | | | | | | | | | |
| Number | 238,872 | 209,303 | 251,578 | 200,853 | 317,012 | 239,865 | - | - | 238,575 | 216,872 |
| MVD | 5.57 | 6.19 | 5.06 | 5.59 | 5.04 | 5.57 | - | - | 4.83 | 5.49 |
| RMSVD | 7.52 | 7.97 | 6.67 | 7.23 | 6.59 | 7.13 | - | - | 6.24 | 6.98 |
| Bias | −1.40 | −1.83 | −0.05 | −0.17 | 0.69 | 0.51 | - | - | −0.93 | −0.53 |
| RMSE | 6.27 | 6.94 | 5.22 | 5.89 | 5.17 | 5.81 | - | - | 4.93 | 5.62 |
| MSPD | 16.97 | 19.77 | 17.68 | 19.52 | 17.29 | 19.27 | - | - | 18.19 | 20.06 |
| Low levels (700–1000 hPa) | | | | | | | | | | |
| Number | 407,126 | 369,908 | 463,477 | 380,543 | 476,166 | 391,224 | - | - | 331,597 | 317,449 |
| MVD | 2.52 | 2.51 | 2.56 | 2.91 | 2.61 | 2.94 | - | - | 2.55 | 2.89 |
| RMSVD | 2.99 | 2.98 | 3.07 | 3.53 | 3.13 | 3.56 | - | - | 3.03 | 3.45 |
| Bias | 1.11 | 1.58 | 0.69 | 0.77 | 0.70 | 0.76 | - | - | 0.54 | 0.83 |
| RMSE | 2.01 | 2.01 | 2.06 | 2.42 | 2.10 | 2.45 | - | - | 2.03 | 2.31 |
| MSPD | 10.09 | 11.74 | 10.67 | 11.87 | 10.67 | 11.90 | - | - | 11.30 | 12.11 |

Table A4. Same as Table A3 except that rawinsonde was used as validation data.

| | CCC | | EBBT & IR/WV | | EBBT | | IR/WV | | CO ₂ | |
|-----------------------------|-------------|-------------|--------------|--------------|-------------|-------------|--------|-------------|-----------------|--------------|
| | Jul. | Jan. | Jul. | Jan. | Jul. | Jan. | Jul. | Jan. | Jul. | Jan. |
| All levels (100–1000 hPa) | | | | | | | | | | |
| Number | 83,148 | 77,797 | 79,179 | 71,497 | 74,819 | 68,925 | 61,418 | 50,244 | 79,135 | 70,147 |
| MVD | 6.22 | 7.04 | 4.88 | 5.38 | 5.26 | 5.62 | 4.99 | 5.18 | 4.90 | 5.25 |
| RMSVD | 7.76 | 8.70 | 6.09 | 7.03 | 6.44 | 7.07 | 6.21 | 6.76 | 6.01 | 6.76 |
| Bias | −1.08 | −1.00 | 0.47 | −0.18 | 0.23 | −0.24 | 0.43 | −0.11 | 0.30 | −0.05 |
| RMSE | 5.98 | 6.95 | 4.57 | 5.74 | 4.83 | 5.75 | 4.67 | 5.37 | 4.56 | 5.45 |
| MSPD | 16.12 | 17.02 | 15.87 | 17.92 | 16.33 | 17.75 | 16.68 | 18.53 | 16.67 | 16.93 |
| High levels (100–400 hPa) | | | | | | | | | | |
| Number | 74,321 | 70,237 | 68,112 | 56,152 | 63,067 | 51,788 | 61,418 | 50,244 | 68,930 | 55,182 |
| MVD | 6.43 | 7.24 | 4.96 | 5.12 | 5.46 | 5.37 | 4.99 | 5.18 | 4.98 | 5.38 |
| RMSVD | 7.95 | 8.91 | 6.16 | 6.67 | 6.64 | 6.59 | 6.21 | 6.76 | 6.10 | 6.96 |
| Bias | −1.19 | −1.23 | 0.44 | −0.08 | 0.17 | −0.10 | 0.43 | −0.11 | 0.32 | −0.28 |
| RMSE | 6.13 | 7.12 | 4.64 | 5.29 | 5.00 | 5.08 | 4.67 | 5.37 | 4.63 | 5.63 |
| MSPD | 16.72 | 17.06 | 16.51 | 18.24 | 17.27 | 18.04 | 16.68 | 18.53 | 17.14 | 17.08 |
| Middle levels (400–700 hPa) | | | | | | | | | | |
| Number | 4374 | 4150 | 6599 | 9124 | 7110 | 10,299 | - | - | 7018 | 7758 |
| MVD | 5.16 | 5.81 | 5.07 | 6.93 | 4.90 | 6.94 | - | - | 4.63 | 5.79 |
| RMSVD | 6.82 | 6.96 | 6.40 | 8.90 | 6.10 | 8.85 | - | - | 5.81 | 7.21 |
| Bias | −0.73 | 0.14 | 0.84 | −0.63 | 0.58 | −0.76 | - | - | −0.08 | 1.19 |
| RMSE | 5.44 | 5.69 | 4.76 | 7.77 | 4.57 | 7.75 | - | - | 4.33 | 5.80 |
| MSPD | 13.73 | 21.67 | 14.46 | 21.14 | 13.37 | 21.17 | - | - | 15.41 | 21.50 |
| Low levels (700–1000 hPa) | | | | | | | | | | |
| Number | 4453 | 3410 | 4468 | 6221 | 4642 | 6838 | - | - | 3187 | 7207 |
| MVD | 3.44 | 3.27 | 3.52 | 4.44 | 3.55 | 4.53 | - | - | 3.45 | 4.00 |
| RMSVD | 4.16 | 3.84 | 4.28 | 5.53 | 4.32 | 5.61 | - | - | 4.22 | 4.93 |
| Bias | 0.34 | 2.25 | 0.46 | −0.48 | 0.47 | −0.49 | - | - | 0.70 | 0.37 |
| RMSE | 2.97 | 2.73 | 3.07 | 4.33 | 3.10 | 4.37 | - | - | 3.02 | 3.79 |
| MSPD | 8.42 | 10.57 | 8.13 | 10.30 | 8.16 | 10.40 | - | - | 9.37 | 10.83 |

Table A5. Comparisons between GK-2A clear-air AMVs for CH08 and GDAPS over the full-disk area for July 2016 and January 2017. The NTC, NTCC methods, and their combination were used for producing GK-2A AMVs, considering QIF > 80. The best scores are in bold and the worst scores are in italics.

| Period | NTC | | NTCC | | NTC & NTCC | |
|---------------------------|-------------|-------------|---------|---------|-------------|-------------|
| | Jul. | Jan. | Jul. | Jan. | Jul. | Jan. |
| High levels (100–400 hPa) | | | | | | |
| Number | 129,345 | 117,342 | 184,248 | 150,169 | 188,629 | 152,996 |
| MVD | 4.68 | 4.73 | 4.75 | 4.80 | 4.58 | 4.67 |
| RMSVD | 6.28 | 6.60 | 6.34 | 6.68 | 6.09 | 6.39 |
| Bias | 0.33 | 0.18 | 0.37 | 0.23 | 0.28 | 0.12 |
| RMSE | 4.71 | 5.03 | 4.88 | 5.15 | 4.85 | 5.10 |
| MSPD | 19.42 | 20.51 | 18.98 | 19.84 | 19.04 | 19.89 |

Table A6. Same as Table A5 except that rawinsonde was used as validation data.

| Period | NTC | | NTCC | | NTC & NTCC | |
|---------------------------|-------|-------|-------|-------|-------------|-------------|
| | Jul. | Jan. | Jul. | Jan. | Jul. | Jan. |
| High levels (100–400 hPa) | | | | | | |
| Number | 11645 | 9750 | 14515 | 10549 | 15170 | 10731 |
| MVD | 5.44 | 6.00 | 5.40 | 5.88 | 5.40 | 5.77 |
| RMSVD | 6.86 | 8.26 | 6.82 | 7.99 | 6.82 | 7.88 |
| Bias | 0.32 | 0.24 | 0.36 | 0.32 | 0.20 | 0.19 |
| RMSE | 5.24 | 6.46 | 5.27 | 6.17 | 5.24 | 6.13 |
| MSPD | 18.75 | 19.48 | 18.09 | 18.73 | 18.31 | 19.02 |

Appendix C. Comparisons of GDAPS and Era-Interim ECMWF Model Data

In this section, we compare GDAPS and Era-Interim ECMWF model data used for the intercomparison of GK-2A and the MTG AMV algorithm. GDAPS and Era-Interim ECMWF U and V profiles are collocated against GK-2A AMVs derived with CLD and CTP from NOAA/NESDIS at 05:40 and 12:10 UTC on 21 July 2016. Table A7 confirms that the collocated ECMWF U and V profiles are more consistent with the corresponding rawinsonde profiles than those of GDAPS.

Table A7. Comparisons of GDAPS and Era-Interim ECMWF model data. They are collocated against GK-2A AMVs with CLD and CTP from NOAA/NESDIS, considering CQIF > 80, at 05:40 and 12:10 UTC on 21 July 2016. Results show that U and V of ECMWF profiles are more consistent with the corresponding rawinsonde than those of GDAPS.

| | ECMWF–GDAPS | GDAPS–Sonde | ECMWF–Sonde |
|--------|-------------|-------------|-------------|
| Number | 84,469 | 2800 | 2800 |
| MVD | 5.61 | 6.14 | 4.31 |
| RMSVD | 7.68 | 8.03 | 5.49 |
| Bias | 0.85 | −0.60 | −0.07 |
| RMSE | 5.77 | 5.14 | 3.73 |

References

1. Menzel, W.P. Cloud Tracking with Satellite Imagery: From the Pioneering Work of Ted Fujita to the Present. *Bull. Am. Meteorol. Soc.* **2001**, *82*, 16. [[CrossRef](#)]
2. Suomi, V.E.; Parent, R.J. A color view of planet earth. *Bull. Am. Meteorol. Soc.* **1968**, *49*, 74–75. [[CrossRef](#)]
3. Oyama, R. Upgrade of atmospheric motion vector derivation algorithms at JMA/MS. *Meteorol. Satell. Cent. Tech. Note* **2010**, *50*, 1–31.
4. Otsuka, M.; Seko, H.; Shimoji, K.; Yamashita, K. Characteristics of Himawari—8 Rapid Scan Atmospheric Motion Vectors Utilized in Mesoscale Data Assimilation. *J. Meteorol. Soc. Jpn.* **2018**, *96B*, 111–131. [[CrossRef](#)]
5. Shimoji, K. The development for MTSAT rapid scan high resolution AMVs at JMA/MS. In Proceedings of the Tenth International Winds Workshop, Tokyo, Japan, 22–26 February 2010.
6. Schmetz, J.; Pili, P.; Tjemkes, S.; Just, D.; Kerkmann, J.; Rota, S.; Ratier, A. An introduction to meteosat second generation (msg). *Bull. Am. Meteorol. Soc.* **2002**, *83*, 977–992. [[CrossRef](#)]
7. Schmetz, J.; Holmlund, K.; Hoffman, J.; Strauss, B.; Mason, B.; Gaertner, V.; Koch, A.; Van De Berg, L. Operational Cloud-Motion Winds from Meteosat Infrared Images. *J. Appl. Meteorol.* **1993**, *32*, 1206–1225.
8. Borde, R.; de Smet, A.; Dew, G.; Watts, P.; Lutz, H.-J.; Carranza, M.; Doutriaux-Boucher, M. AMV extraction algorithm in preparation for MTG. In Proceedings of the Eleventh International Winds Workshop, Auckland, New Zealand, 20–24 February 2012.
9. Nieman, S.J.; Menzei, W.P.; Hayden, C.M.; Gray, D.; Wanzong, S.T.; Velden, C.S.; Daniels, J. Fully Automated Cloud—Drift Winds in NESDIS Operations. *Bull. Am. Meteorol. Soc.* **1997**, *78*, 1121–1134. [[CrossRef](#)]
10. Daniels, J.; Bresky, W.; Wanzong, S.; Velden, C.; Berger, H. *GOES-R Advanced Baseline Imager (ABI) Algorithm Theoretical Basis Document for Derived Motion Winds*; NOAA NESDIS Center for Satellite Applications and Research; University of Wisconsin-Madison: Madison, WI, USA, 2019; p. 98.
11. Daniels, J.; Velden, C.; Bresky, W.; Irving, A.; Turner, K. Status and development of GOES wind products at NOAA/NESDIS. In Proceedings of the 6th International Winds Workshop, Madison, WI, USA, 7–10 May 2002; pp. 71–80.
12. Bedka, K.M.; Velden, C.S.; Petersen, R.A.; Feltz, W.F.; Mecikalski, J.R. Comparisons of Satellite-Derived Atmospheric Motion Vectors, Rawinsondes, and NOAA Wind Profiler Observations. *J. Appl. Meteorol. Climatol.* **2009**, *48*, 1542–1561. [[CrossRef](#)]
13. Lee, E.; Kim, Y.; Sohn, E.; Cotton, J.; Saunders, R. Application of hourly COMS AMVs in KMA operation. In Proceedings of the 11th International Winds Workshop, Auckland, New Zealand, 20–24 February 2012.
14. Sohn, E.H.; Chung, S.R.; Park, J.S. Current status of COMS AMV in NMSC/KMA. In Proceedings of the 11th International Winds Workshop, Auckland, New Zealand, 20–24 February 2012; pp. 16–20.

15. Lee, S.; Song, H.-J. Quantifying the inflation factors of observation error variance for COMS and MTSAT Atmospheric Motion Vectors considering spatial observation error correlation. *Q. J. R. Meteorol. Soc.* **2017**, *143*, 2625–2635. [[CrossRef](#)]
16. Oh, Y.; Kim, J.H.; Park, H.; Baek, K. Development and Analysis of COMS AMV Target Tracking Algorithm using Gaussian Cluster Analysis. *Korean J. Remote Sens.* **2015**, *31*, 531–548. [[CrossRef](#)]
17. Choi, Y.-S.; Ho, C.-H. Earth and environmental remote sensing community in South Korea: A review. *Remote Sens. Appl. Soc. Environ.* **2015**, *2*, 66–76. [[CrossRef](#)]
18. Bessho, K.; Date, K.; Hayashi, M.; Ikeda, A.; Imai, T.; Inoue, H.; Kumagai, Y.; Miyakawa, T.; Murata, H.; Ohno, T.; et al. An Introduction to Himawari-8/9—Japan’s New-Generation Geostationary Meteorological Satellites. *J. Meteorol. Soc. Jpn.* **2016**, *94*, 151–183. [[CrossRef](#)]
19. Borde, R.; García-Pereda, J. Impact of Wind Guess on the Tracking of Atmospheric Motion Vectors. *J. Atmos. Ocean. Technol.* **2013**, *31*, 458–467. [[CrossRef](#)]
20. García-Pereda, J.; Borde, R. The Impact of the Tracer Size and the Temporal Gap between Images in the Extraction of Atmospheric Motion Vectors. *J. Atmos. Ocean. Technol.* **2014**, *31*, 1761–1770. [[CrossRef](#)]
21. Cho, H.-J.; Sohn, E.-H.; Ou, M.-L. The impact of target box size on wind speed biases in satellite-derived atmospheric motion vectors. In Proceedings of the 2008 EUMETSAT Meteorological Satellite Conference, Darmstadt, Germany, 8–12 September 2008.
22. Deb, S.K.; Wanzong, S.; Velden, C.S.; Kaur, I.; Kishitawal, C.M.; Pal, P.K.; Menzel, W.P. Height Assignment Improvement in Kalpana-1 Atmospheric Motion Vectors. *J. Indian Soc. Remote Sens.* **2014**, *42*, 679–687. [[CrossRef](#)]
23. Borde, R.; Dubuisson, P. Sensitivity of Atmospheric Motion Vectors Height Assignment Methods to Semitransparent Cloud Properties Using Simulated Meteosat-8 Radiances. *J. Appl. Meteorol. Climatol.* **2010**, *49*, 1205–1218. [[CrossRef](#)]
24. Nieman, S.J.; Schmetz, J.; Menzel, W.P. A Comparison of Several Techniques to Assign Heights to Cloud Tracers. *J. Appl. Meteorol.* **1993**, *32*, 1559–1568. [[CrossRef](#)]
25. De Smet, A. AMV height assignment with Meteosat-9: Current status and future developments. In Proceedings of the 9th International Winds Workshop, Annapolis, MD, USA, 14–18 April 2008.
26. Hocking, J.; Rayer, P.; Rundle, D.; Saunder, R.; Matricardi, M.; Geer, A.; Brunel, P.; Vidot, J. *RTTOV v11 Users Guide*; NWC SAF Report; Met Office: Exeter, UK, 2015.
27. Fritz, S.; Winston, J.S. Synoptic use of radiation measurements from satellite tiros ii. *Mon. Weather Rev.* **1962**, *90*, 1–9. [[CrossRef](#)]
28. Menzel, W.P.; Smith, W.L.; Stewart, T.R. Improved Cloud Motion Wind Vector and Altitude Assignment Using VAS. *J. Clim. Appl. Meteorol.* **1983**, *22*, 377–384. [[CrossRef](#)]
29. Holz, R.E.; Ackerman, S.; Antonelli, P.; Nagle, F.; Knuteson, R.O.; McGill, M.; Hlavka, D.L.; Hart, W.D. An Improvement to the High-Spectral-Resolution CO₂-Slicing Cloud-Top Altitude Retrieval. *J. Atmos. Ocean. Technol.* **2006**, *23*, 653–670. [[CrossRef](#)]
30. Borde, R.; Doutriaux-Boucher, M.; Dew, G.; Carranza, M. A Direct Link between Feature Tracking and Height Assignment of Operational EUMETSAT Atmospheric Motion Vectors. *J. Atmos. Ocean. Technol.* **2013**, *31*, 33–46. [[CrossRef](#)]
31. Holmlund, K. The Utilization of Statistical Properties of Satellite-Derived Atmospheric Motion Vectors to Derive Quality Indicators. *Weather Forecast.* **1998**, *13*, 1093–1104. [[CrossRef](#)]
32. Imai, T.; Uesawa, D. Clear Sky Radiance (CSR) product derived from Himawari-8 data. *Meteorol. Satell. Cent. Tech. Note* **2016**, *61*, 53–58.
33. Tokuno, M. Improvements in the method to extract operational cloud motion winds and water vapor motion winds of the GMS-5 system. In Proceedings of the 4th International Winds Workshop, Saanenmoser, Switzerland, 20–23 October 1998; pp. 61–68.
34. Marshall, J.L.; Pescod, N.; Seaman, B.; Mills, G.; Stewart, P. An Operational System for Generating Cloud Drift Winds in the Australian Region and Their Impact on Numerical Weather Prediction. *Weather Forecast.* **1994**, *9*, 361–370. [[CrossRef](#)]
35. *MTG-FCI: ATBD for Atmospheric Motion Vector Product*; EUMETSAT: Darmstadt, Germany, 2011.
36. Le Marshall, J.; Rea, A.; Leslie, L.; Seecamp, R.; Dunn, M. Error characterisation of atmospheric motion vectors. *Aust. Meteorol. Mag.* **2004**, *53*, 123–131.

37. Menzel, W.P. Report from the working group on verification statistics. In Proceedings of the Third International Winds Workshop, Ascona, Switzerland, 10–12 June 1996; pp. 17–19.
38. Bresky, W.C.; Daniels, J.M.; Bailey, A.A.; Wanzong, S.T. New Methods Toward Minimizing the Slow Speed Bias Associated with Atmospheric Motion Vectors. *J. Appl. Meteorol. Climatol.* **2012**, *51*, 2137–2151. [[CrossRef](#)]



© 2019 by the authors. Licensee MDPI, Basel, Switzerland. This article is an open access article distributed under the terms and conditions of the Creative Commons Attribution (CC BY) license (<http://creativecommons.org/licenses/by/4.0/>).